Cryo-electron tomography reveals enrichment and identifies microtubule lumenal particles in neuronal differentiation

Saikat Chakraborty[1]*, Antonio Martinez-Sanchez[1,2,3], Florian Beck[1], Mauricio Toro-Nahuelpan[4,5], In-Young Hwang[6], Kyung-Min Noh[6], Wolfgang Baumeister[1], Julia Mahamid[4]*

[1]Deptartment of Molecular Structural Biology, Am Klopferspitz 18, Martinsried 82152, Germany

[2]Institute of Neuropathology & Cluster of Excellence "Multiscale Bioimaging: from Molecular Machines to Networks of Excitable Cells" (MBExC), University Medical Center Göttingen, 37075 Göttingen, Germany.

[3]Current Address: Dept. of Computer Sciences & Heath Research Institute of Asturias (ISPA), University of Oviedo, 33007 Oviedo, Spain

[4]Structural and Computational Biology unit, European Molecular Biology Laboratory, Meyerhofstrasse 1, 69117 Heidelberg, Germany

[5]Current address: Santiago GmbH & Co. KG, Willich, Germany.

[6]Genome Biology unit, European Molecular Biology Laboratory, Meyerhofstrasse 1, 69117 Heidelberg, Germany

Correspondence: chakraborty@biochem.mpg.de, julia.mahamid@embl.de

Key words: Neuronal cytoskeleton; Neuronal differentiation; Microtubules; Lumenal particles; Lattice damage; Primary neurons; Induced pluripotent stem cells; *In situ* cryo-electron tomography; Subtomogram averaging; Spatial statistics;

Summary:

Functional architecture of the neuronal microtubule (MT) cytoskeleton is maintained by various MT-associated proteins (MAPs), most of which bind to the MT outer surface. Yet, electron microscopy (EM) has long revealed hitherto unknown electron-dense particles inside the lumens of neuronal MTs. Here, we use cryogenic electron tomography (cryo-ET) to analyze the native three-dimensional (3D) structures and organization of MT lumenal particles inside vitrified rodent primary neurons, pluripotent P19 cells and human induced pluripotent stem cell-derived neurons. We obtain 3D maps of several lumenal particles at molecular resolution that periodically decorate neuronal MTs. We show that increased lumenal particle localization is concomitant with neuronal differentiation and correlates with higher MT curvatures. Lumenal particles binding topology in MTs, their structural resemblance to tubulin binding cofactors (TBCs), enrichment around MT lattice defects and at plus-ends indicated their potential role in tubulin proteostasis for the maintenance of neuronal MTs.

Introduction:

The neuronal MT cytoskeleton plays an obligatory role in neuronal morphogenesis during development with its ability to support synaptic trafficking (Hirokawa et al., 2010), signal transduction (Akhmanova and Steinmetz, 2008), axon guidance (Cooper, 2013) and synapse formation (Jaworski et al., 2009). MTs are also essential for maintaining polarized morphologies of the neurons (Bentley and Banker, 2016); irregularities affecting MTs lead to abnormal morphogenesis and ultimately to detrimental neurodevelopmental defects (Bulinski, 2019; Larti et al., 2015; Srivastava and Schwartz, 2014). Thus, the neuronal MT cytoskeleton is carefully maintained by complex layers of regulatory mechanisms that include a large pool of neuron specific MAPs (Bodakuntla et al., 2019). These cellular factors bind to the MT lattice and regulate the dynamics and materials properties of the MT cytoskeleton in different contexts, such as during cell cycle and differentiation (Amos and Schlieper, 2005; Drewes et al., 1998). So far, *in vitro* structural studies of MT-MAP interactions (Manka and Moores, 2018) have shown that these MAPs, almost exclusively, bind to the outer surface of the hollow MT. There is little evidence of MAPs binding to the MT lumenal surface, except for small molecules such as Taxol (Nogales et al., 1999). On the other hand, early conventional EM studies illuminated the presence of periodically arranged electron-dense particles within the MT lumen of heavy metal stained samples of insect epithelia (Bassot and Martoja, 1966), spermatids (Afzelius, 1988) and blood platelets (Behnke, 1967). Such lumenal particles appeared to be most abundant in various neuronal cells. Recent cryo-ET studies have unambiguously confirmed the presence of such particles within the MT lumen of non-fixed frozen sections of different cells and neurons (Bouchet-Marquis et al., 2007; Chakraborty et al., 2020a; Foster et al., 2022; Garvalov et al., 2006; Hoffmann et al., 2021; Schrod et al., 2018). However, till date, none of these studies has revealed details about their molecular identities, the nature of their association with MT lumen, their distribution along MTs or function. Thus, with an ever-growing number of MAPs being identified as organizers or regulators of the MT cytoskeleton, there is a gap in our understanding of the complexity of MT-MAP interactions in their native environment within neuronal cells.

The MT lumen, with a diameter of approximately 17 nm, is largely excluded from the cytoplasmic environment except for lateral pores that form upon severing and/or defects, and the two filament ends. Theoretical modeling predicts very slow diffusion of molecules through the MT lumen (Odde, 1998). Nevertheless, regulation of MT stability by selective localization of MAPs or posttranslational modification (PTM) inside the MT lumen may provide a favorable mechanism, since these processes would not interfere with the multitude of trafficking events happening on

the MT outer surface. Such regulation is indeed supported by studies of MT inner-proteins (MIPs) found inside the lumen of specialized doublet MTs in cellular appendages such as cilia and flagella. MIPs maintain the structural integrity of the MT lattice during extreme mechanical deformations caused by ciliary or flagellar beatings (Ichikawa et al., 2019; Owa et al., 2019). However, the role of MIPs in intracellular MTs remains poorly described. Instead, MT mechanical stability is known to be regulated by acetylation of lumenal K-40 of alpha-tubulin by Tubulin Acetyltransferase (TAT) (Akella et al., 2010; LeDizet and Piperno, 1987). K-40 acetylation weakens lateral interactions between protofilaments (pF), making MTs more flexible and limiting lattice damage in long lived MTs (Portran et al., 2017; Xu et al., 2017). Post mitotic neurons are long lived and undergo complex morphological transitions including intricate arborization to adapt to new functional demands. This requires the underlying MT cytoskeleton to be flexible, yet very stable to maintain functional neuronal architecture. Not surprisingly, acetylated MTs are an integral part of axonal MT bundles that are used as highways for transport (Katrukha et al., 2021). Therefore, TATs have long been thought to be a component of the lumenal particles (Gaertig and Wloga, 2012; Topalidou et al., 2012). Several studies also implied that deacetylases such as HDAC6 access the MT lumen by hitchhiking on the MT plus-end tracking protein EB1 for removing lumenal acetylation marks (Matsuyama et al., 2002; Zilberman et al., 2009). A recent report suggested MAP6 could be also a component of MT lumen that performs similar functions as MIPs in doublets by stabilizing a coiled architecture of neuronal MTs (Cuveillier et al., 2020). However, there are no direct structural evidences that show these prospective candidates are part of lumenal particles inside neurons.

In this study, we utilized *in situ* cryo-ET to elucidate the molecular architectures and organization of lumenal particles in vitrified rodent primary hippocampal neurons, human induced pluripotent stem cells (hiPSC)-derived neurons and murine pluripotent or differentiated P19 cells. Towards that, we have adapted a recently described template-free particle detection procedure (Martinez-Sanchez et al., 2020) to develop automated particle picking for subtomogram averaging (STA) (Grünewald et al., 2003) and elucidated *in situ* structures of several types of lumenal particles at molecular resolution that periodically decorate neuronal MTs. Combined with quantitative spatial statistical tools (Martinez-Sanchez et al., 2022) for cryo-tomograms, we quantitatively analyzed the concentrations and organizations of each particle type with nanometer-scale precisions within the MT lumens of the different neuronal cells. We show ultrastructural changes inside the MT lumen associated with increasing concentrations and tighter packing of lumenal particles during neuronal differentiation. A correlation between mechanical bending of MTs and abundance of lumenal particles was established, highlighted by the spatial clustering of particles near exposed

MT lattice sites, potentially indicating their protective role in maintaining MT lattice integrity. Thus, our study suggests that MT lumenal particles are an integral part of the differentiated neuronal MT cytoskeleton and are involved in MT homeostasis.

Results:

Organization of lumenal particles within MTs

Cryo-tomographic slices of vitrified thin processes (thickness <0.5 µm) of rodent primary hippocampal neurons revealed tightly bundled neuronal MTs wrapped inside membrane-bound processes, along with sparsely populated vesicular organelles and other macromolecules (**Fig. 1A, movie S1**). Densely packed, globular particles within the lumen were clearly distinguishable (**Fig. 1A, B**). We established the polarity of the MTs using STA, which revealed mixed MT polarity in the bundle (**Fig. 1B, Fig. S1A-D)**. MT bundles with mixed polarities are signatures of vertebrate dendrites (Yau et al., 2016), indicating the neuronal process in **Fig**. **1A** is likely a dendritic process. The persistent presence of lumenal particles in all MTs irrespective of their orientations indicated no apparent relation between lumenal particles distribution and MT polarity. Further, STA provided a 8.2 Å *in situ* map of MTs (**Fig. 1C, S1E-F**) with discernible secondary structural features. The MTs were constituted of 13 pFs (inset, **Fig.1B**), indicating that the presence of lumenal particles did not affect the pF numbers in mammalian neurons, contrary to the proposed 15 pFs in nematode touch receptor neurons (Topalidou et al., 2012) or MT-based appendages (Ichikawa and Bui, 2018). Tomographic slices from murine pluripotent P19 cells and hiPSC-derived neurons (**Fig. 1D**) revealed varying abundances of MT lumenal particles, with particle being more spaced apart compared to those of the primary neuronal MTs (**Fig. 1D, S2A-F, Movie S2-S3**) (Garvalov et al., 2006). Morphologically, pluripotent P19 lumenal particles appeared different and smaller in size compared to the primary and hiPSC-derived neurons, hinting at localization of different types of particles in a cell-type specific manner.

In order to quantitatively describe the lumenal particle abundances, MTs were segmented from the cryo-tomograms using a generic cylinder template (Chakraborty et al., 2020b; Rigort et al., 2012). We developed an automated method for reliably detecting lumenal particles inside the segmented MT lumens in an unbiased, template-free image processing procedure (**Fig. S3A-B**, **Movie S1-S3**, see methods) by employing discrete Morse theory segmentation and the topological persistence simplification (Martinez-Sanchez et al., 2020). Using this method, precise particle concentrations (particles per μm^3 of the lumenal volume) within each MT lumen was measured (**Fig. 1E**). In accordance with the visual inspection, it revealed the highest concentration of lumenal particles present in the primary neurons, as noted in earlier studies

(Echandía et al., 1968; Garvalov et al., 2006), followed by that in hiPSC-derived neurons (**Fig.1E**). In case of pluripotent P19 cells, concentration distribution (grey violin, **Fig.1E**) was clearly bimodal, indicating at least two populations of MTs and/or cells containing different amounts of particles. However, neighboring MTs within the same P19 cellular processes were observed to contain markedly different concentrations, indicating particle distribution was not uniform within the MTs of the same cell (**Fig. S2D** inset).

Next, we quantified packing of the lumenal particles by measuring the nearest-neighbor (NN) distances using the particle coordinates refined in REgularised LIkelihood OptimisatioN (RELION) (Scheres, 2012) (see later) as described before (Martinez-Sanchez et al., 2020). We observed a sharp distribution in case of primary neurons with the most frequent NN-distance of ~ 12 nm (**Fig. 1F**), followed by smaller peaks at 16 and 20 nm. This suggested periodic arrangement of particles within neuronal MTs as observed in **Fig.1D**. In line with this, we observed a clear linear correlation (Pearson's r = 0.97) between the number of particles contained in each MT and MT length in neurons (**Fig. S3C**) indicating maximum packing efficiency. The NN-distance distributions in pluripotent P19 and hiPSC-derived neurons were centered on 8-10 nm, albeit with lower frequencies and skewed towards longer distances, indicating that an 8 nm periodicity was not always maintained. Since 8 nm is roughly the size of a tubulin dimer (**Fig. 1C**), and the observed distances were multiples of 8, we speculated that the lumenal particles could be positioned along with the tubulin dimers. We statistically evaluated these spatial patterns for higher order organization using Ripley's L function (Ripley, 1988) against complete randomness using the numerical corrections for cryo-tomograms (Martinez-Sanchez et al., 2020) (**Fig. S3D**-**F**). While positive values of L function indicate spatial clustering, negative values indicate uniform distribution, given it is separated from the complete randomness. Negative L function observed for lumenal particles thus indicated a uniform distribution of the lumenal particles in the primary and hiPSC-derived neurons (**Fig. S3D**-**F**).

Native 3D morphologies of lumenal particles

Next, we sought to elucidate the structures of the lumenal particles using the automated detection of particle coordinates, followed by computational particle extraction and STA (**Table S1**). The subtomograms initially exhibited marked structural and compositional heterogeneity that limited convergence of the averages. In order to generate homogeneous particle groups, they were subjected to several rounds of 3D classification followed by 3D auto-refinement in RELION. Reproducibility of the results were confirmed by 3D refinements of each class average against different initial models, including simple sphere and/or cylinder (**Fig. S4A-H**). Class averages

were obtained de novo, *i.e.* by reference-free analysis and contained sufficient range of views (**Fig. S4B**). However, all analyzed particles were relatively small, with an overall size of 7-10 nm, posing a significant challenge for STA-based structure determination. Their approximate molecular masses measured from the tomograms were found to be in the range of 200-400 kDa (**Fig. S5A-F**). These particle masses corroborated the notion that MT lumen could contain up to 350 kDa proteins with a diameter of ~10 nm. The size and molecular mass of these particles safely precluded a classical motor–cargo complex.

Visual analyses of the pluripotent P19 tomograms suggested two types of particles, based on their association with the MT wall; a subset of the particles show distinct connections with the MT wall, while others seem to be floating inside the lumen. STA supported the visual inspection (**Fig. 2A; Fig. S4D,G; Table S1**). In the MT-wall bound category, the most notable class averages in P19 cells were found to be elongated particles with four apparent domains arranged in crisscross fashion. We called this 'bound MT inner protein 1' or bMIP1 and bMIP2, found to attach to the MT wall with thin stalk-like densities (**Fig. 2A**). The distance between the neighboring stalks was found to be ~4 nm. Therefore, it could be envisaged that they could stabilize MT structure by 'crosslinking' protofilaments. A third bound density, bMIP3 has a multi-lobe globular structure bound to the MT lumen wall via three stalk-like densities. A fourth class average (bMIP4) bore similarity with the bMIP2 with the difference that it was bound to the MT lumen with one stalk and with extra density on its top. Therefore, these two molecules could be related. All bMIPs were found exclusively in the pluripotent P19 cells, with bMIP2 and bMIP1 having the highest and lowest abundances, respectively (**Fig.S6A**). Among all the analyzed and refined particles, the fraction of MT bound and free particles was close to 1:1.

The floating particles (hence forth, fMIP) from all cell types appeared predominantly globular and often contained a hollow core (**Fig. 2B-C; Fig.S4C,E**). The bulk of the averaged densities were located centrally in the MT lumen. Yet, the absence of contact between the particles and the MT wall does not preclude contact site, either because of their disposition along the missing wedge in tomographic data (Lučić et al., 2013) or they are too flexible to converge into a discrete density in the average maps. Within the fMIPs, a common feature in the different neuronal cells was the presence of a distinct ring like structure (fMIPs 1, 6, 9, 11, 13). Small globular densities were found to be attached to the ring-shaped base, hinting they could be multiprotein complexes (e.g. fMIP6, 9). There were also structures that are relatively smaller and distinct from the ring containing structures, possibly representing different conformations of the same molecule or have similar constituents with different oligomeric state (e.g. fMIP3, 10, 14). Nevertheless, the presence

of common structural features of fMIPs across different neuronal cell hinted that fMIPs could be involved in general MT related processes. These fMIPs, however, have varied abundances in different neuronal cells. Among ring-like structure containing fMIPs, fMIP1, 6, and 9 have similar abundances in pluripotent P19 and primary neuron (**Fig.S6A-B**), while fMIP13 has the highest abundance in hiPSC-derived neuron (**Fig.S6C**). Notably, unlike all other MIPs analyzed, fMIP13 and 15 showed regular arrangements within the MT lumen with nearest-neighbors positioned at 8 nm distance and/or multiples thereof (**Fig.S6D**).

Taxol treatment alters lumenal particle distribution

In order to identify the molecular constituents of lumenal particles, we sought a way to manipulate particle concentrations within MT lumen to enable a proteomics-based analysis. Since a substantial population of the lumenal particles in pluripotent P19 cells were bound to MT lumen, we wondered whether Taxol binding could affect bMIPs distribution. Thus, pluripotent P19 cells were treated with 5 µM Taxol for 30 mins prior to vitrification and visualized using cryo-ET. Particle concentrations in the Taxol-treated samples were found to be visibly reduced compared to the control (**Fig. 3A, S7A-B, MovieS4**) with concomitant increase in the inter-particle distance (**Fig. 3B**). In order to find out which population of MIPs were affected, we analyzed relative abundances of each class averages in control and Taxol treated samples. A distinct shift in populations of the MIPs in Taxol treated cells was observed, where wall-bound particles became the predominant fraction (**Fig. 3C**). Notably, bMIP1 concentration was found to be significantly higher and almost exclusive in Taxol treated P19 cells (**Fig. 3D**). The concentrations of the rest of the bMIPs were significantly reduced compared to the control. The concentrations of fMIPs, on the other hand, were found to be very low following Taxol treatment supporting visual inspection that revealed limited presence of centrally located particles within MT lumen. Comparison between NN-distances of bMIP1 between control and treated samples revealed change in bMIP1 organization within the lumen in presence of Taxol. In treated cells, bMIP1 has now more neighbors at 8 nm distance compared to the control, indicating bMIP1 bound to MT lumen in a more regular manner and possibly in small clusters (**Fig. 3E**).

A subset of fMIPs are potential tubulin binding cofactors

We used the Taxol-induced selective reduction in the fMIP concentrations to identify molecular components using a differential enrichment of interacting proteins in control and Taxol-treated cells by affinity purification-MS (AP-MS) based proteomics. We took advantage of the previously described mitotic HeLa Kyoto cells expressing GFP tagged β-tubulin (Chakraborty et al., 2020b;

Poser et al., 2008). These cells can be grown in large quantities suitable for large scale pulldowns. Importantly, Taxol-induced reduction in particle concentration is recapitulated there as well (**Fig. 3F; Fig. S7C-D**). This confirmed particle concentration reduction was associated with the properties of Taxol, not with the cell line. β-tubulin was isolated by affinity purification using anti-GFP antibody immobilized on magnetic beads (**Fig. S7E**) from intracellularly crosslinked control DMSO-treated cells and Taxol-treated cells. Cross-linking ensured preservation of all particles interacting with MTs during isolation procedure. A volcano plot visualized the differentially enriched proteins identified by mass spectrometry, displaying their statistical significance based on their t-test with peptide level abundance. We found that Taxol treatment significantly reduced the abundance of over 150 proteins, including several MAPs known to bind the MT outer surface, such as Esconsin and MAP1S (**Fig. S7F-G**). Notably, we observed also modest reduction of three cytosolic tubulin binding cofactors (TBC): Tubulin binding cofactor A (TBCA), D (TBCD) and E (TBCE) ($P < 0.05$) (**Fig. S7G**).

Next, we scanned the electron microscopy database (EMDB) for EM maps of the AP-MS candidate proteins for structural similarity with our *in situ* lumenal particles density maps. Most *bona fide* structural MAPs, such as MAP7, in our proteomics inventory are predicted to have disordered extended structures and therefore do not have any similarity with our maps (Al-Bassam et al., 2002; Ferro et al., 2020; Kellogg et al., 2018). However, the ring-shaped maps were found to bear striking similarities to the tubulin binding cofactor-D (TBCD, mass 132 kDa, EMD-6390), one of the tubulin binding cofactors involved in folding and degradation of β-tubulin (**Fig. 4A-C**) (Tian and Cowan, 2013). HEAT repeats of the TBCD form an alpha solenoid, whose EM density map structurally resembles a ring (Nithianantham et al., 2015). Therefore, we used an AlphaFold-2 (Jumper et al., 2021) prediction of human TBCD and aligned it with yeast Cse1p that has been known to fit TBCD EM density (Nithianantham et al., 2015) using flexible alignment method (Li et al., 2020). The distinct alpha solenoid ring structure of the obtained TBCD fitted well the ring-shaped base of the fMIP1, 9 and 13 (correlation coefficients > 0.8, green, **Fig**. **4A-C**). Previous biochemical evidences indicated TBCD can exist in a stable complex with ADP ribosylation factor-like protein 2 (Arl2) (Tian et al., 2010) as well as with β-tubulin (Francis et al., 2017). A β-tubulin model adequately fitted in the remaining globular density of fMIP9 with a correlation coefficient of 0.85 (yellow, **Fig**. **4A)**. Therefore, the fMIP 9 tentatively represent a binary complex between TBCD and β-tubulin with a projected mass of ~180 kDa. In case of fMIP1, Arl2 model (PDB 1KSH) dimensionally fitted well within the globular density indicating a complex between TBCD and Arl2 (light pink, cc value 0.9, **Fig**. **4C)** with a minimum projected mass of ~150 kDa. The mass of these complexes corroborate with our mass measurements directly from the

tomograms (**Fig.S5F**). The U-shaped density with two globular heads of fMIP5 (cyan, **Fig**. **4D**) bore structural resemblance to the EM density of TBCE, another cofactor that binds α-tubulin, obtained by negative stain single particle EM study of purified proteins (Serna et al., 2015). The globular heads likely correspond to the Cap-Gly (PDB 1WHG) and UBL domains (PDB 4ICV). The Cap-Gly domain binds to the globular density that is very well fitted by α-tubulin (in yellow, with cc 0.88, **Fig**. **4D,** PDB 1TUB)**,** and importantly also places the tubulin binding loop close to the tubulin C-terminal. The curved segment between the globular heads dimensionally fits well with the TLR4 (**Fig**. **4D)** that structurally mimics the TBCE LRR domain (cc 0.94, PDB 3RJ0). Therefore, we present a likely case where tubulin-bound tubulin cofactors are present inside MT lumen. Among TBCD-containing fMIPs, fMIP13 from hiPSC-derived neurons have the highest relative abundance, making up to 25% of the total lumenal particles population, indicating their potential involvement in important function in MT biology (**Fig. 4B**).

Increased MT lumenal particle localization during neuronal differentiation

Observation of densely packed MT lumen exclusively in neuronal cells (**Fig.1A-B, D**) (Garvalov et al., 2006) raises question as to whether such an arrangement of lumenal particles is structurally integral to neuronal MTs. In order to address this question, we took advantage of the ability of pluripotent P19 cells to differentiate into neuron-like cells *in vitro* and subsequently followed structural change within the MT lumen. The neuronal precursor cells undergo major morphological changes during differentiation into mature neurons, primarily driven by the underlying MT cytoskeletal to develop axons and dendrites (Falconer et al., 1989a). Neurospheres generated after aggregation of the P19 cells upon exposure to 0.5 µM retinoic acid (RA) were allowed to differentiate for about 2 weeks. Neurons were selectively grown using DNA synthesis inhibitor. When these *in vitro* differentiated neurons were imaged using cryo-ET, thin processes revealed polar array of MT bundles along with other cytoskeletal filaments reminiscent of hiPSC-derived neurons (**Fig**. **5A**). Unlike in pluripotent P19 cells, the MT bundles were frequently observed embedded in a dense intermediate filament network (**Fig. 5B**), characteristics of a neuron (Falconer et al., 1989b). It further revealed significantly higher concentration of particles (**Fig. 5C**), relative to their parental state, that are arranged in an ordered array with 8 nm NN-distance (**Fig. 5C-E**). However, their concentration was slightly lower than in the rodent primary neurons. We examined whether there was preferential enrichment of a particular luminal particle subset in the *in vitro* differentiated neurons. Quantification of concentrations showed that after differentiation, both bMIP4 and fMIP4 were enriched ~1.5 times compared to undifferentiated state inside the MT lumen (**Fig. 5F**). Modest enrichments were observed for other fMIPs, while the remaining

bMIPs were maintained at similar level. Therefore, both bMIP4 and fMIP4 could play a role in altering MT properties that facilitate MT cytoskeleton to adapt to neuron specific functions.

Lumenal particle abundance correlates with MT curvature

We wondered whether enrichment of lumenal particles in differentiated cells is linked with observable physical properties of MTs. Since bMIPs bind to the pFs, one could envisage that they could stabilize curved MT lattice. A similar hypothesis has been put forward for MAP6 that stabilizes coiled MTs in neurons (Cuveillier et al., 2020). Therefore, we sought to find if there is any link between MT curvature and lumenal particle concentration.

We determined the extent of MT curvature in neurons using the tangent-correlation length ($^{a}L_p$), as described in our previous work (Chakraborty et al., 2020b). Cryo-tomograms revealed curved MTs inside neuronal shafts with segments exhibiting sinusoidal trajectories and twisted parallel MT bundles that create a helical path with occasionally one MT writhing around the bundle (**Fig. 6A**). This type of MT arrangement has been recently described in haptonema, a MT-based motile organ of a haptophyte algae (Nomura et al., 2019). The distributions of tangent-correlation lengths corresponding to primary neurons showed that neuronal MTs were highly curved with a mean value of 28.4±3.4 µm, indicating they were in a compressed state (top margin, **Fig. 6B, D**). In contrast, for pluripotent P19 MTs, $^{a}L_p$ distribution was broad with two major peaks centered on ~17 and ~42 µm with a mean $^{a}L_p$ of 41.6±5.33 µm (top margin, **Fig. 6C**). The heterogeneous curvature distribution resolved upon P19 differentiation into neurons *in vitro* into a single peak centered predominantly on 25.9±3.9 µm, at par with the curvatures found in primary neurons (top margin**, Fig. 6D**). We next examined whether a correlation exists between MT curvature and its lumenal particle concentration. A 2D correlation revealed in primary neurons, highly curved MTs contained higher particle concentration (**Fig. 6B**). In pluripotent P19 cells, a distinct segregation was observed where all highly curved MTs contained high particle concentration (similar to primary neurons) (**Fig. 6C**) and vice versa. However, upon differentiation P19 cells a similar trend as in **Figure 6B** was observed. This correlation hints at two important aspects: localization of lumenal particles within the MT lumen might be related to MT curvature and hence possibly linked with mechanical forces known to regulate neuronal differentiation (Vining and Mooney, 2017).

Lumenal particles form nanocluster around partially broken MT lattice

Lumenal particle enrichment in curved MTs raises speculations about their possible role. It is thought that lumenal particles, including TATs, gain entry into the lumen through curvature induced lattice breaks (Coombes et al., 2016). If this is true, we would expect an increase in the

particle abundance at the breaks. However, it is also possible that weakly bound or floating lumenal particles could be lost from the MT lumen through the breaks, thereby decreasing the particle abundance.

Since enrichment of lumenal particles in curved MTs is clearly distinguishable in pluripotent P19 cell neurites, we examined whether they pertain to partially broken and exposed lattice regions. We pinpointed several partially broken MTs where MT lattices suffered from loss of one or several protofilament segments (**Fig. 7A**). We created a 'lattice map' of one such representative case using STA, where individual subtomograms were mapped back to the original positions in the tomogram and color coded according to the cross-correlation coefficient (CCC) (**Fig. 7B-C**). CCC-values near the broken site were lower, indicating flexibility of tubulins in this region (**Fig. 7C**). Visual inspection revealed presence of tightly packed, regular array of lumenal particles spanning the broken MT lattice, contrary to the randomly distributed particles in the intact MTs (**Fig. S3E**). Particles within the MT were counted and represented as a color coded spatial occupancy map. Such representation highlighted micro-cluster formation spanning the broken region compared to the intact part (**Fig. 7D,** red segment). We used bivariate Ripley's L function to derive statistical significance of such clustering (Martinez-Sanchez et al., 2020). In this case, distances between the particles and break points were measured and compared with complete randomness using Monte Carlo simulation. Experimental median of the L function displayed bell shaped curve with positive values (green line, **Fig. 7E**) and away from the random simulation (gray area, **Fig. 7E**), indicating cluster formation was statistically significant (**Fig. 7E**). This further showed that the size of this domain was ~300 nm around the lattice breaks. Additionally, we observed clusters of ribosomes around the exposed lattices. Spatial arrangement of several of these ribosomes conformed the geometry of a helical polysome configuration (**Fig. 7D-inset, S5G-I,** see methods), indicating they could be translationally competent. The lumenal particles present at the broken region were thus exposed to the cytosol (**Fig. 7C)** and in close proximity to the polysomes. Taken together, we show a complex molecular interface exist at the partially exposed MT lattices in pluripotent P19 cells. Similar MTs in interphase HeLa cells were found and devoid of such molecular complexity (not shown).

Lumenal particles accumulate near the plus end of polymerizing MTs

Exposed MT lattice could act as a gateway for accessing the MT lumen as suggested by the presence of tightly packed nanoscale cluster of lumenal particles. We wondered whether such clustering happens at the open MT plus-ends, another possible entry point for lumenal particles. To this end, fresh MT polymerization was initiated in pluripotent P19 cells using the MT-

depolymerizing drug, Nocodazole, followed by wash-off as described in the methods. Particle concentration was lower in newly polymerized MTs compared to the control (**Fig. 7F**). This indicated that particle population has yet to reach a steady state. Cryo-tomograms from these samples showed several MT plus-ends identified from their flared morphology (**Fig. 7G-I, MovieS5**). Remarkably, we observed presence of clusters of lumenal particles near the plus end of the MTs, with larger inter-particle space further along the MT length (**Fig. 7H**, inset). We measured the occupancy of lumenal particles using a kernel along the length of three representative MTs and color coded the MTs based on the obtained particle occupancy. It revealed clusters near the plus-end as dictated by the red band signifying higher particle occupancy that shifted gradually along the MT length from the plus-end. This indicates re-entry of particles as small clusters within MTs that were at different time points in their assembly. We statistically evaluated such clustering of particles using the previously described bivariate Ripley's L function from the plus-end compared with the spatial randomness. Although visually clear, such test only revealed a weak tendency of the particles to form clusters with domain size up to 200 nm from the plus end (see **Fig. S8A-B** for details). Nevertheless, particles were more tightly packed with a mean inter-particle distance of 9.6±3.4 nm within ~100 nm from the plus-end compared to the distal regions towards the minus-end (mean distance 14.3±6.7 nm) (**Fig. S8C**). STA revealed freshly polymerizing MTs accumulated similar classes of both bMIPs and fMIPs albeit at lower concentrations from the cytosol as they grow, corroborating the visual inspection of tomographic slices. Among the class averages, concentrations of bMIP3, fMIP1 and 2 have specifically reduced with a greater fold-change in this sample (**Fig.S8D**). Since freshly polymerized MTs are highly curved, the elevated levels of lattice defects observed in these MTs (Chakraborty et al., 2020b) could be related to the overall reduction in the concentration of the MIPs.

Discussion

The presence of lumenal particles inside MTs has been known since decades (Afzelius, 1988; Bassot and Martoja, 1966; Behnke, 1967; Bouchet-Marquis et al., 2007; Cyrklaff et al., 2007; Garvalov et al., 2006). Yet, our understanding of the molecular components of these particles and their functions remained elusive. It is an open question whether MT lumenal particles represent novel types of MAPs involved in modulating MT stability. Alternatively, it was suggested that lumenal particles could be globular proteins or mRNA that are stored or transported inside MTs (Burton, 1984; Echandía et al., 1968). We leveraged the power of *in situ* cryo-ET to perform an extensive molecular-resolution structural survey of lumenal particles within the native MTs of

various neuronal cells. Towards that, we adapted an automated template-free particle detection and picking procedure for MT lumenal particles (Comaniciu and Meer, 2002; Martinez-Sanchez et al., 2020). We applied these methods in conjunction with cryo-ET and STA that allowed us to extract useful novel structural, spatial and biological information about MT lumenal particles.

A key feature specific to neuronal MTs was the periodic decoration of the MT lumen by particles. Such specific neuronal decorations led us to speculate that lumenal particles are involved in emergent behavior of neuronal MTs (Reber and Hyman, 2015). It is not unlikely given that extensive mechanical forces are exerted on neuronal MTs during neuronal development (Javier-Torrent et al., 2021; Vining and Mooney, 2017) and due to their primary role in vesicular trafficking (Hirokawa et al., 2010), and axon migration (Dent et al., 2011). We found neuronal MTs have highly curved appearances irrespective of the cell types under study (**Fig. 6A**). Therefore, to maintain MT structural integrity, neuronal MTs possess distinct physico-chemical properties as revealed by the complex tubulin-code they carry and a number of distinct structural MAPs such as MAP2 and Tau (Subramanian and Kapoor, 2012) that stabilize them (Bodakuntla et al., 2019). It is possible that the lumenal particles could also endow similar additional emergent properties to neuronal MTs, as they are well placed to structurally stabilize MT lattice from the lumenal side without hampering motor traffic on the outer surface. Such a mechanism, in fact, operates in ciliary doublet MTs that are coated with a network of MIPs to protect MT integrity during mechanical deformations (Owa et al., 2019).

The densities we resolve for bMIPs have potential to crosslink several protofilaments together via multiple stalk-like densities from the lumenal side. Such binding mode is likely to hold protofilaments together during mechanical deformations (**Fig. 2A**), and therefore alter the materials' property of the MTs. MAP6, an intrinsically disordered protein with three MT stabilizing Mn modules is thought to operate in a similar manner and stabilize curved neuronal MTs (Cuveillier et al., 2020). We indeed observed emergence of highly curved MTs during the course of differentiation of pluripotent P19 cells that correlated with enhanced abundances of bMIPs. Interestingly, a non-uniform distribution of curvature was found in pluripotent P19 neurites with a clear tendency to accumulate more particles within the more curved MTs. This hinted at the existence of MT subtypes in pluripotent cells possessing different mechanical properties. Spatially segregated existence of MT subtypes in neurons is known and generally thought to arise from distinct PTMs and/or of distinct tubulin isotypes (Katrukha et al., 2021). It remains to be seen whether lumenal particle localization happen selectively to those MTs that are destined to be neuronal processes and hence experience mechanical forces over other MTs in different regions.

While bMIPs could exert their effect on MTs directly by binding to the pFs, fMIPs are probably involved in regulating MT constituents or dynamics. Some of our 3D maps showed common features of these fMIPs and suggested that they likely have common constituent: TBCs, monomeric tubulin and Arl2. TBCs are mainly involved in 'tubulin proteostasis', from proper folding of the tubulin monomers, formation of tubulin heterodimers, to tubulin degradation (Lewis et al., 1997; Lundin et al., 2010). Thus, presence of TBC bound tubulin complexes within the lumen could have fascinating implications and raise speculations about their possible functions. TBC bound tubulin complexes might be involved in maintaining a tubulin pool, thereby creating a "tubulin transport chain'' to provide/make fresh tubulin dimers for growing MTs required for growth cone expansion and maintenance of synapses. In support of this, we spotted very few ribosomes in axonal processes in agreement with protein synthesis in axons being rare (Lasek et al., 1973). Furthermore, tubulins are transported from the cell body to distant neurites at very slow speed of 0.1-3 mm/day (Campenot et al., 1996). In such scenario, it might not be surprising if TBC bound tubulins packed within the MT lumen could invoke local tubulin proteostasis to make fresh dimers for incorporation at the plus-end of MTs and/or to the lattice defects in the distal regions of neurons. On the other hand, MT disruption by bare TBCD is known to be regulated by Arl2 through complex formation (Bhamidipati et al., 2000). Therefore presence of TBCD:Arl2 complex might ensure maintenance of MT cytoskeletal integrity inside neurons (Tian et al., 2010). Thus, we envisage fMIPs could impact MT homeostasis within neurons.

The presence of cluster of lumenal particles at partially broken MT lattice suggests a protective role in curved MTs. Highly curved neuronal MTs are likely to accumulate extensive nanoscale lattice defects (Atherton et al., 2018; Chakraborty et al., 2020b; Srayko et al., 2006). Generally, depolymerization of defective MTs, either due to their intrinsic ability or by the action of severing enzymes, and polymerization of a new set of MTs has been regarded as the main mechanism for maintaining a functional MT network. However, such wholesale replacement mechanism could disrupt functionality of neuronal MTs. In such scenario, bMIPs could stabilize the cracked MT lattice by forming micro-domains around the defect and holding the surviving pFs together. Formation of such micro-domain indicates that particles might move inside the lumen. Since lattice defects might act as a good substrate for regulatory ATPases such as Katanin (Davis et al., 2002), bMIPs clusters could also antagonize their function and provide sufficient time for self-repair to kick in. Similar protective role has been recently proposed for the CLASPs that relocalize to the bent MT regions and stabilize them (Aher et al., 2020). fMIPs could invoke local tubulin homeostasis, provide fresh tubulins for MT repair and remove damaged tubulins. Most importantly, self-repair maintains the complex 'tubulin code' that is a requirement for regulating

long term MT-dependent traffic. Our findings could further shed light on the role of impaired tubulin proteostasis in generating defective MT network in severe neuro-developmental defects such as giant axonal neuropathy (Wang et al., 2005), hyperparathyroidism (Parvari et al., 2002), inherited early-onset encephalopathy (Flex et al., 2016) and infantile neurodegeneration (Edvardson et al., 2016). Taken together, the MT lumen might serve as a transport channel as hypothesized previously (Burton, 1984; Echandía et al., 1968) as well as an important regulator of MT mechanics in neurons.

In summary, we have elucidated native structures of a subset of MT lumenal protein complexes and suggested molecular identities for a number of these complexes. We suggest that lumenal particles are involved in maintaining MT lattice integrity under compressive cellular forces during neuronal differentiation that also include local tubulin homeostasis. Thus, our data highlights novel emergent behavior of the cytoskeleton occurring through interactions between MTs and lumenal particles in the complex environment of neurons.

ACKNOWLEDGMENTS

We thank Ina Poser and A. Hyman for providing the HeLa cell lines, C. Papantonio and C. Capitanio of the Baumeister lab for providing rodent primary neuron culture, the MPI Biochemistry mass spectrometry core facility for proteomics support, and Arsen Petrovic for valuable suggestions regarding homology modeling. S.C. was supported by a Max Planck Society fellowship. A.M.-S. was supported by the Deutsche Forschungsgemeinschaft (DFG, German Research Foundation) under Germany's Excellence Strategy - EXC 2067/1- 390729940. M.T-N and I.H were supported by a fellowship from the EMBL Interdisciplinary Postdoctoral Program (EI3POD) under Marie Skłodowska-Curie Actions COFUND. W.B. acknowledges support from the Center for Integrated Protein Science, Munich. J.M. acknowledges funding from the EMBL.

AUTHOR CONTRIBUTIONS

S.C, W.B and J.M designed the research. S.C. performed sample preparation, cell biological and biochemical analysis, cryo-ET on P19 and rodent primary neuron and subtomogram averaging for all data; J.M provided mitotic HeLa tomograms; A.M.-S developed automated particle picking procedure, spatial statistical tools and helped data analysis; F.B. provided computational support, helped data analysis. M.T-N and J.M collected hiPSC data; K.M.N and I.H cultured hiPSC neurons; S.C. J.M. and W.B. wrote the manuscript with contribution from all authors.

DECLARATION OF INTERESTS

W.B. is on the Thermo Fisher Scientific life sciences advisory board. All authors declare no conflict of interest.

DATA AVAILABILITY

Tomograms included in this manuscript and all maps generated in this work are deposited in the EMDB. Tomogram preprocessing and particle picking (PySeg) scripts are available in GitHub. (https://github.com/williamnwan/TOMOMAN;https://github.com/anmartinezs/pyseg_system)

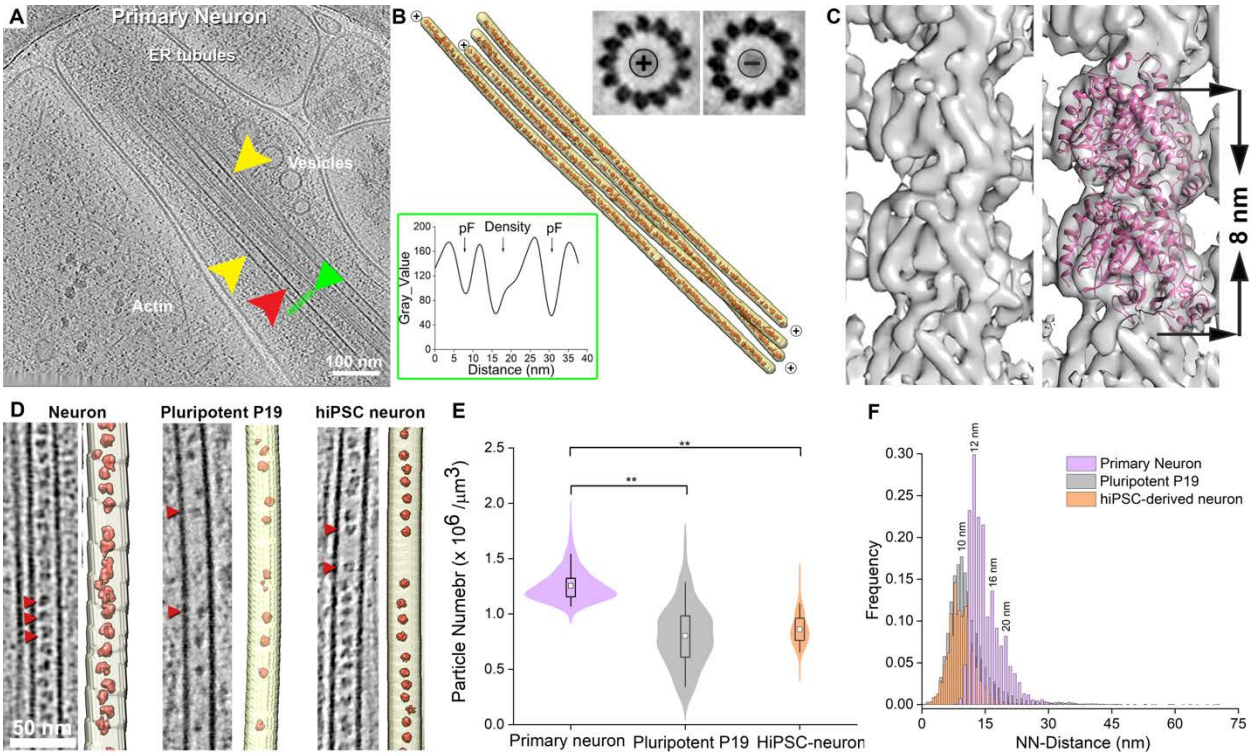

Figure 1: **Organization of lumenal particles inside neuronal MTs**. **A**. 9 nm thick tomographic slice of a rodent hippocampal neuronal process showing MT bundle (yellow arrowhead) containing stacked lumenal particles (red arrowhead). Other macromolecules and membranous organelles indicated. Inset (green frame): line profile across a MT indicated by green arrowhead revealing presence of extra density between pFs. **B**. 3D rendering of traced MTs (yellow) and lumenal particles (red). MT plus-ends are indicated by plus sign. Inset: Subtomogram averages of individual MTs shows different polarity. **C**. 8.2 Å *in situ* subtomogram average of the 13 pF rodent primary neuronal MTs, and with fitted tubulin dimer (right). Dimension of a tubulin dimer indicated. **D.** Tomographic slices showing varying particle abundances in the indicated cell types. Segmentations of the MTs (Yellow) and lumenal particles (red) are shown. **E.** Quantification of the particle concentrations in different cell types presented in (D) represented as boxplot within a violin. Mean values are marked by the black box. Asterisks indicate Mann-Whitney test **: significance P<0.01. **F**. Nearest-neighbor distance distributions of the lumenal particles in indicated cell types.

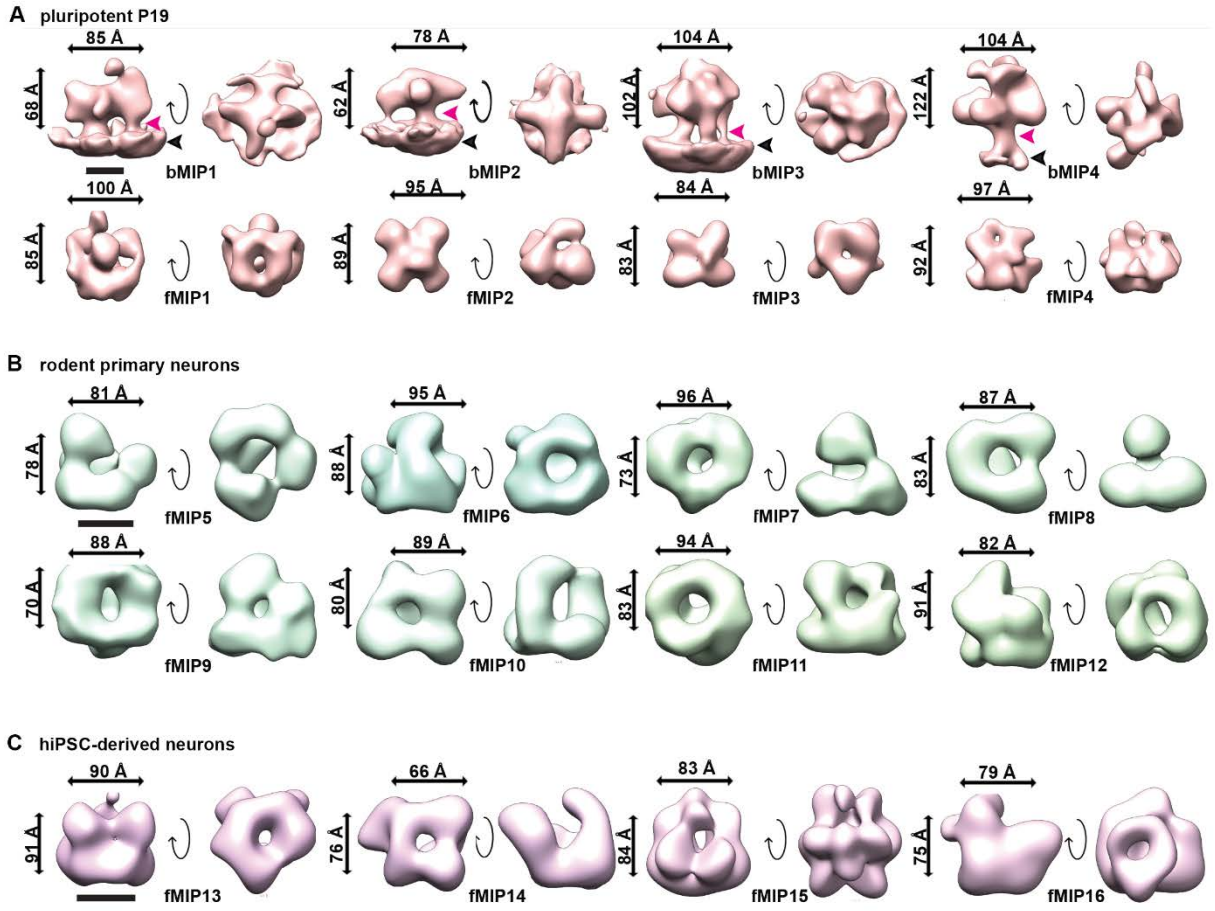

Figure 2: Subtomogram averages of lumenal particles in P19, primary and hiPSC-derived neurons. A. Class averages (in brown) from the pluripotent P19 cells. MT wall-bound class of particles indicated by their attachment to MT lumen (bMIP; black arrowhead) with stalk like density (pink arrowhead). **B**, **C**. Class averages of lumenal particles found in primary neurons (green) and hiPSC-derived neurons (purple). Scale bars 5 nm. Two-sided arrows indicate maximum dimensions of the maps. Curved arrow indicate 90° rotation.

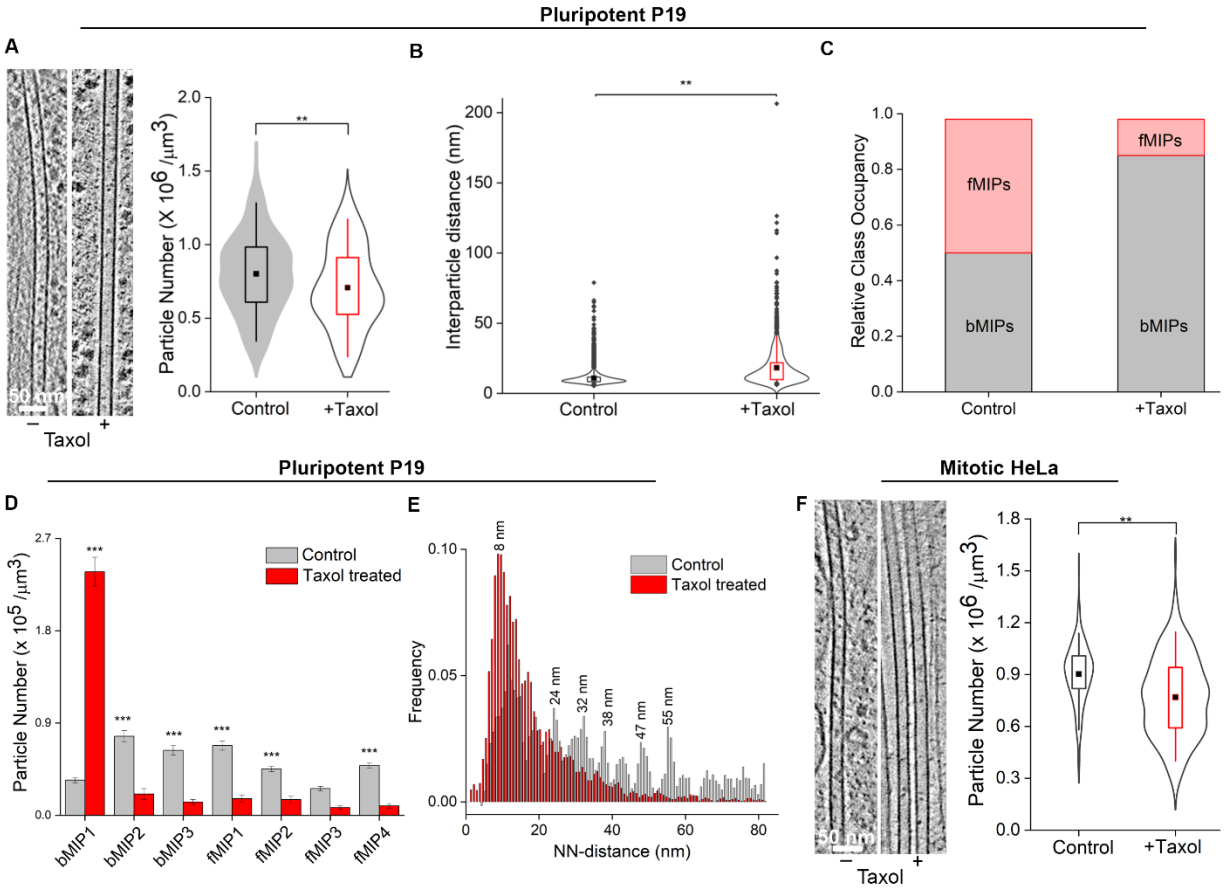

Figure 3: Taxol treatment reduces lumenal particles concentration. A. 6.8 nm thick tomographic slices of control and Taxol-treated pluripotent P19 cells showing particle distribution inside MT lumen. Quantification of particle concentrations for samples presented in (A) shown as combination of box-plot and data distribution in violin plot. Box in the middle denotes mean. Statistical significance done using Mann-Whitney test, **p<0.01. **B**. Interparticle distances in control (black box) and Taxol treated pluripotent P19 cells (red box), Black box indicates mean. **C**. Relative abundance of wall-bound (bMIPs) and floating (fMIPs) category of class averages in control and Taxol treated pluripotent P19 samples. **D**. Concentrations of the class averages in control and Taxol treated pluripotent P19 cells. Error bar indicates standard error of mean (SEM). Statistical significance ***p<0.001, obtained by two-sample t-test. **E**. NN-distance distribution of bMIP1 in control and Taxol treated pluripotent P19 cells. Peaks corresponding to distances are indicated. **F**. 9 nm thick tomographic slices of control and Taxol-treated mitotic HeLa cells showing particle distribution inside MT lumen. Quantification of particle concentrations shown as in (A). Box in the middle denotes mean. Statistical significance done using Mann-Whitney test, **p<0.01.

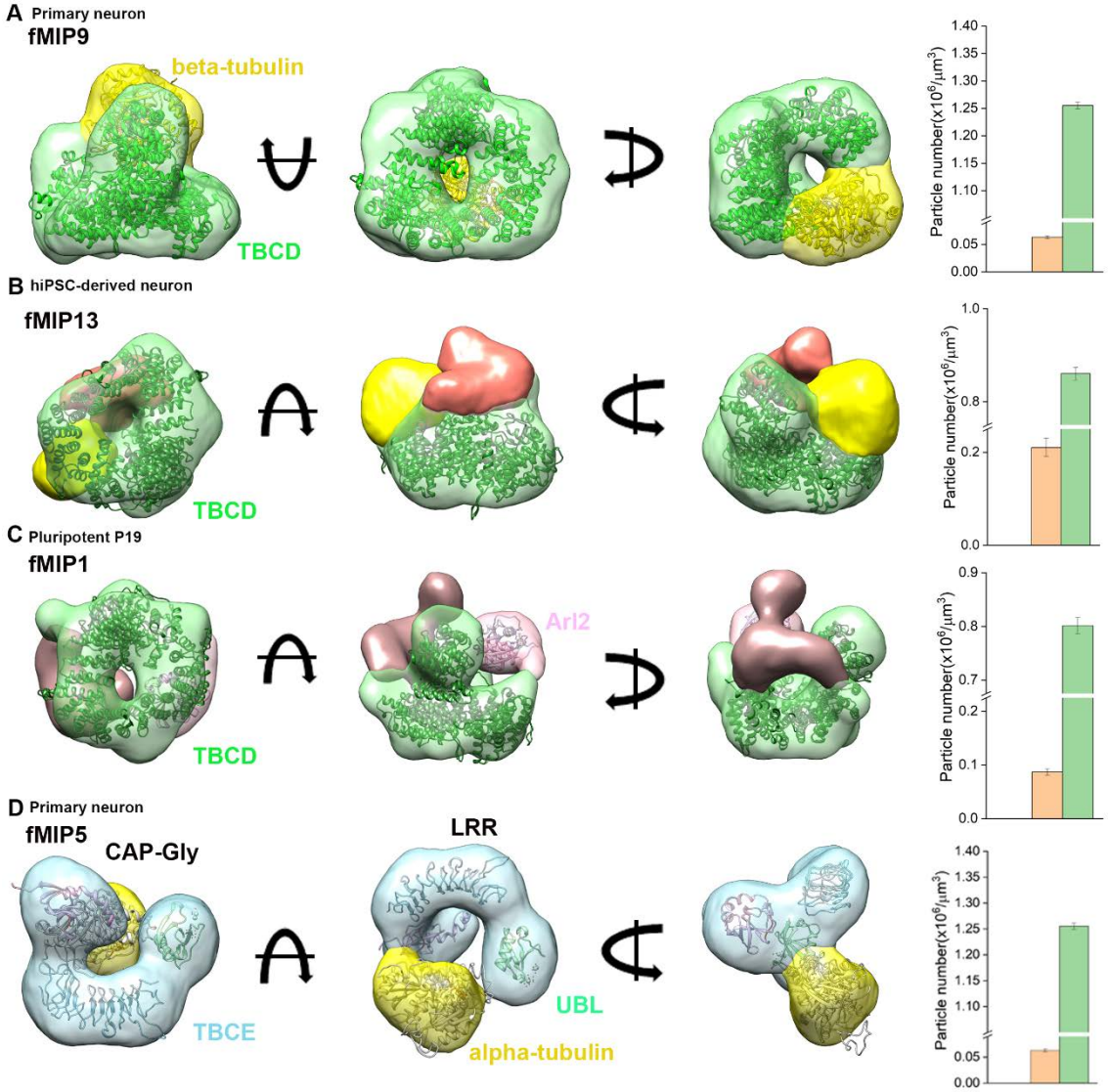

Figure 4: A subset of fMIPs resemble tubulin-binding cofactors. A. Segmented map of fMIP9 from primary neurons shown in three views. The ring-shaped base (green) is fitted with HEAT repeats of human TBCD (green). Yellow globular density is fitted with β-tubulin. **B**. Segmented map of fMIP13 from hiPSC-derived neurons shown in three views. The ring-shaped base (green) is fitted with HEAT repeats of human TBCD (green). Remaining densities (red and yellow) are unassigned. **C**. Segmented density map of fMIP1 from pluripotent P19 cells shown in three views. The ring-shaped base (green) is fitted with HEAT repeats of human TBCD (green). Light pink globular density is fitted with the GTPase, Arl2. Remaining density (brown) is unassigned. **D**. Segmented map of fMIP5 from primary neurons shown in rotated views. The U-shaped base (cyan) is fitted with LRR, and two globular head domains are fitted with UBL and CAP-Gly domains of TBCE as indicated. Yellow globular density is fitted with α-tubulin. In all cases, bar-graphs represent abundance of the corresponding fMIPs (orange) compared to total number particles (green). Error bar indicates SEM.

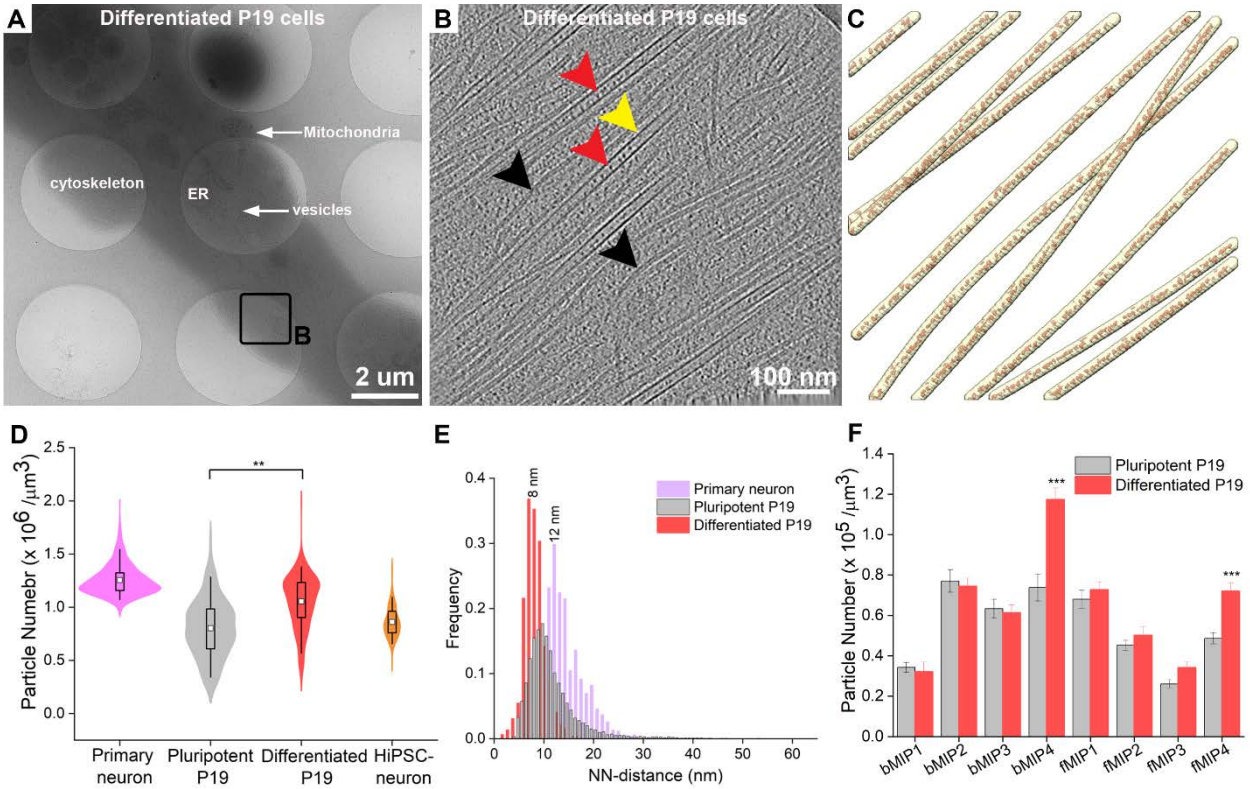

Figure 5: **Induction of neuronal differentiation enhances MT lumenal particles**. **A**. A neuronal process of differentiated P19 cell at 10 DIV on EM grid, showing dense cellular organelles and a polarized cytoskeleton. **B**. 9 nm thick tomographic slice of differentiated P19 cells showing MTs (yellow arrowhead) containing stacked lumenal particles (red arrowhead), and parallel array of Intermediate filaments (gray arrowhead). **C**. 3D rendering of traced MT filaments. MTs (yellow), lumenal particles (red). **D.** Quantification of the particle concentrations in the indicated cell types, represented as boxplot within a violin. Mean values are marked by a box. Asterisks indicate Mann-Whitney test **: significance P<0.01. **E**. NN-distance distributions of the lumenal particles in pluripotent and differentiated P19 cells. **F**. Comparison between the concentrations of each class averages before and after differentiation. Error bar indicates SEM. Statistical significance ***p<0.001, obtained by two-sample t-test.

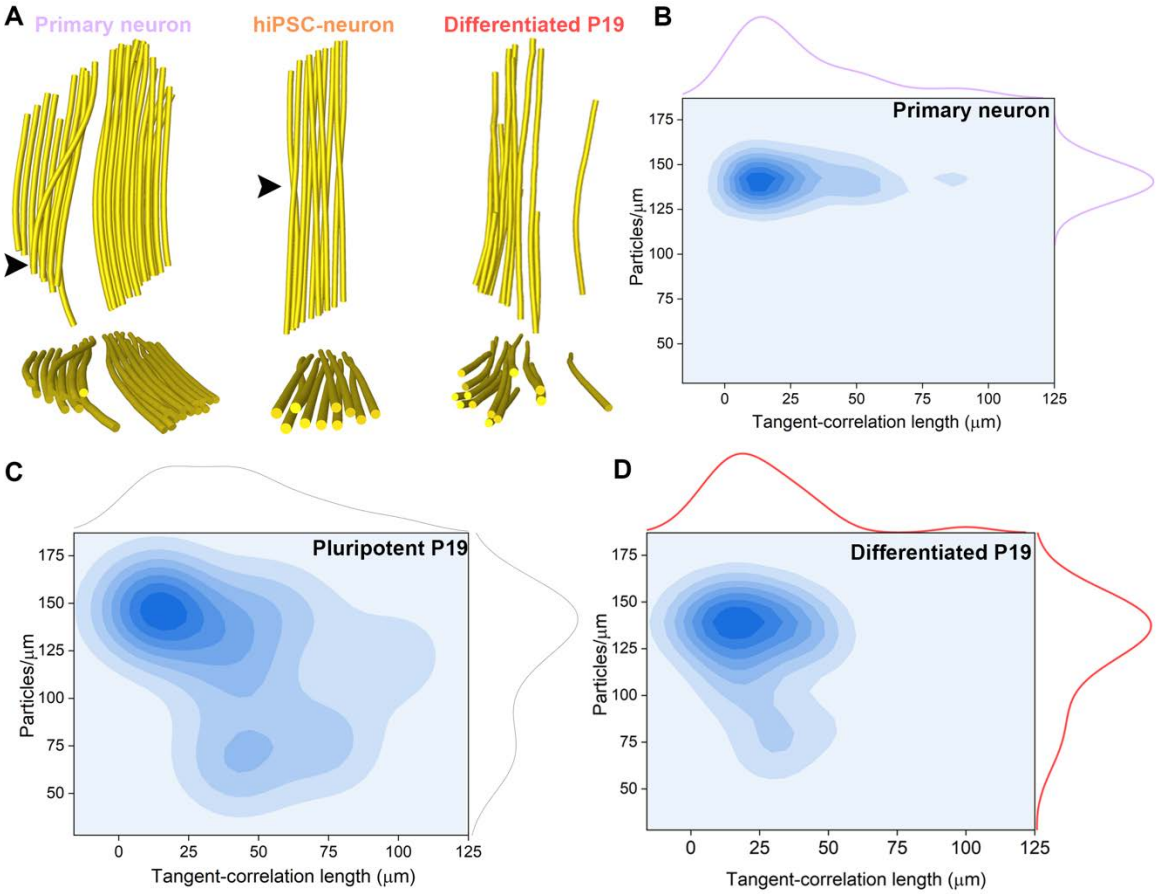

Figure 6: MT curvature correlates with lumenal particle density. A. Representative 3D rendering of MT bundles from a primary, hiPSC and differentiated P19 derived neuronal process. Top, x-y views, bottom, x-z views. Black arrows indicate MTs displaying curved trajectory. **B-D.** Distribution plots of tangent-correlation lengths ($^{a}L_p$) and mean particles per micron for **B**) primary neurons (magenta) (N=40), **C)** pluripotent P19 cells (gray), (N=24), and **D**) differentiated P19 neurons (red) (N=26), shown on the margins. Correlation between the $^{a}L_p$ and mean particles per micron indicated as contours for the indicated cell types. N, denotes numbers of tomograms analyzed.

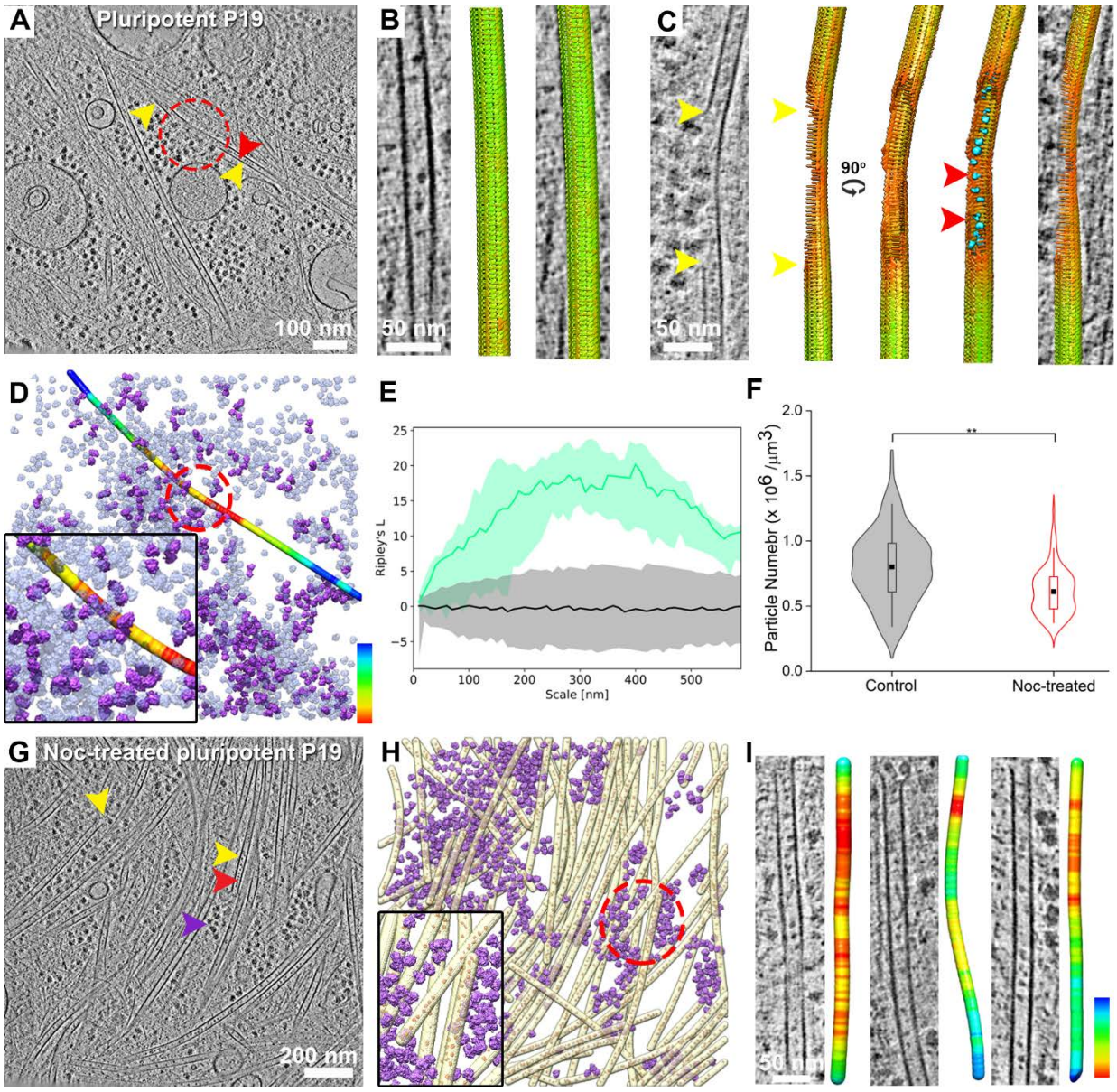

Figure 7: Lumenal particles cluster at the lattice breaks and MT plus ends. A. 6.8 nm thick tomographic slice of a pluripotent P19 MTs showing a broken MT (yellow arrowheads and red circle, enlarged in C). Red arrowhead indicates lumenal densities. **B**. 6.8 nm thick tomographic slice of an intact pluripotent P19 MT along with lattice map superimposed. Subtomograms are shown as an arrow and CCC values are color coded where green represent highest CCC. **C**. Similar to B, but for a partially broken MT lattice (between yellow arrowheads). Lattice maps shows missing subtomograms in the damaged regions. 3D-surface rendered lumenal particles (cyan) are mapped back in the exposed MT region. **D**. Surface rendered image of the tomogram in A, with the single MT color coded with lumenal particle occupancy where red represent highest abundance. Ribosomes shown as transparent violet. Polyribosomes cluster around the broken MT lattice shown in violet. Inset is a zoomed image of the interface (red circle). **E**. Bivariate Ripley's L function for the particles clusters found at the partially broken MT lattices (N=20) (green line). Black line indicate median of the L function for a set of random particle distributions and the

grey shaded area represent the intervals of confidence in range of [5, 95]%. **F**. Quantification of particle concentrations in control and freshly polymerized MTs of pluripotent P19 cells. Statistical significance by Mann-Whitney test **P<0.01. **G**. 6.8 nm thick tomographic slices of showing particle distribution inside freshly polymerized MT lumen. Arrowheads indicate plus-end of MTs (yellow), lumenal particles (red), and ribosomes (violet). **H**. 3D surface rendering of panel G showing the dense MT network (yellow) along with lumenal particles (red) interspersed with ribosomes (violet). Inset is an enlarged region of MT plus-end (red circle). **I**. Representative slices of plus-end (top side) of freshly polymerized MTs of pluripotent P19 cells with corresponding color coded occupancy map of lumenal particles along the MT length.

Materials and Methods

Primary neuron culture

Rat hippocampal neurons were derived from postnatal day 1–2 rats in accordance with the procedures accepted by the Max Planck Institute for Biochemistry. Briefly, the embryo tissue was minced in HBSS-HEPES buffer and trypsinized for 15-30 mins to collect hippocampal neurons as described elsewhere (Fukuda et al., 2015; Lučić et al., 2007). Briefly, collected neurons were washed with DMEM and 10% FBS, and were plated on 35 mm dishes at the density of 5×10^5 cells each containing four/five poly-L-lysine coated R1/4 SiO_2 Quantifoil grids. Cells were kept in an incubator at 37 °C and 5% CO_2 for ~4 h. Then the grids were transferred to a culture dish containing pre-conditioned B27 medium and a glial feeder cell layer. After 3 days from seeding, cytosine β-D-arabinofuranoside (Ara-C) (SIGMA, C1768) was added (final 5 µM) to the culture dish to stop glial cell duplication. Neurons were cultivated for 10–18 days. One third of the culture medium was exchanged once a week. Grids were vitrified on day 12 using a Vitrobot Mark 4. The Vitrobot was set to 37°C, 90 % humidity, blot force 10, blot time of 10 s and 2 s drain time.

P19 cell culture and differentiation

Pluripotent murine P19 cells were cultured in P19 growth medium (P19GM) containing alpha-MEM (Gibco, 12571063) supplemented with nucleosides 10% (v/v) FBS (Thermo Fisher, 16000036), 100 mg/mL each of penicillin and streptomycin (Gibco, 15140122) at 37°C with 5% CO_2.

Pluripotent P19 cells were induced to differentiate into neuronal cells in induction medium (P19IM) containing 95% alpha-MEM and 5% FBS. Briefly, cells were collected after trypsinization with 0.05% trypsin and re-suspended in P19IM medium. Cells were then allowed to aggregate in a low binding petri-dish in presence of 0.5 µM all-trans retinoic acid (SIGMA, R2625-50MG). Aggregates of P19 cells formed within 2 days and further continued for another 2 days with a fresh P19IM containing RA. Aggregates were then harvested and treated with 0.05% trypsin (Gibco, 25300054) and DNase (50 µg/mL) (New England Biolabs GmbH, M0303S) followed by resuspension in P19GM. Cells were plated in 35 mm poly-L-lysine tissue culture dishes at a density of 5×10^5 cells each containing four poly-L-lysine coated R2/1 Au Quantifoil grids. Ara-C (SIGMA, C1768) was added at 5 mM concentration after 2 days and culture continued for 7-10 days. Grids were vitrified on day 10.

Sample preparation was essentially same as described before (Chakraborty et al., 2020b). Briefly, Pluripotent P19 cells were grown on plasma cleaned, UV sterilized Gold Quantifoil grids (R2/1, Au 200 mesh grid) that had an additional 20 nm carbon. Cells were kept in an incubator overnight to allow adhesion, followed by vitrification by plunge freezing using a Vitrobot Mark 4 (FEI). In all cases, Vitrobot was set to 37°C, 95 % humidity, blot force 10, blot time of 10 s and 2 s drain time.

HeLa cell culture, grid preparation and micromachining

HeLa Kyoto cells expressing both green fluorescent protein (GFP)-tagged β-tubulin and mCherry tagged histone (H2B-mCherry), were cultured at 37°C with 5% CO_2 in Dulbecco's modified Eagle's medium (DMEM) (Gibco, 31966021) containing 10% (v/v) fetal bovine serum (FBS) (Gibco, 16000036), 2 mM L-glutamine, 100 mg/mL penicillin, 100 mg/mL streptomycin, and 0.5 mg/mL geneticin (G418) (Gibco, 10131019). Mitotic cells were prepared using thymidine (Sigma, T1895-5G) block as described before (Chakraborty et al., 2020b).

For the preparation of mitotic HeLa cells, naturally mitotic or mitotically synchronized cells were detached from the culture flask by mechanical shake off, and the collected medium was centrifuged at 300 g for 2 min to concentrate the cell pellet. 4 µL of the cell suspension was deposited onto plasma cleaned holey carbon-coated 200 mesh copper R 2/1 grids followed by vitrification by plunge freezing using a Vitrobot Mark 4 (FEI) using similar conditions as in P19 sample preparation. Plunge-frozen grids fixed into custom-made autogrids were mounted into a 45°-pre-tilted shuttle and micro-machined using a dual-beam (FIB/SEM) microscope (Quanta 3D FEG, FEI) as described before (Chakraborty et al., 2020b; Mahamid et al., 2016). For improved conductivity of the final lamella, we sputter coated the grid after cryo-FIB preparation with platinum in the Quorum prep-chamber (10 mA, 1 s).

hiPSCs culture and neuronal differentiation

Human iPSCs (male CESCG-297) were kindly provided by Michael Snyder's laboratory at Stanford University. hiPSCs were derived from peripheral blood mononuclear cells following Institutional Review Board (IRB) approval and Stem Cell Research Oversight (SCRO) approval at Stanford University and under informed consent. hiPSCs were maintained below passage 40, regularly tested for mycoplasma (assayed with Mycoplasma PCR Detection Kit, iNtRON), and examined genome integrity (using low coverage whole genome sequencing). hiPSCs were cultured in vitronectin (ThermoFisher, A14700) coated dish (0.5 µg/cm^2) with Essential 8 medium with supplement (ThermoFisher, A1517001). For neuronal differentiation, we adapted and modified published methods that generate excitatory neurons using rapid Neurogenin-2 (NGN2)

induction (Ho et al., 2016; Zhang et al., 2013). Briefly, hiPSCs were transduced with TetO-hNGN2-P2A-eGFP-T2A-PuroR and rtTA lentivirus at 60% of confluency (Day 0). After 24 h, the virus-containing medium was washed away and replaced with 1:1 ratio of Neurobasal A (ThermoFisher, 10888022) and DMEM/F12 medium containing GlutaMAX, Insulin (Gibco, 51300-044), N2/B27 without Vitamin A (ThermoFisher, 17502048/12587010) supplements, and 1 µg/ml of doxycycline to activate TetO promoter (Day 1). hiPSCs expressing hNGN2-P2A-eGFP-T2A-PuroR were selected by adding 3 µg/ml puromycin (Day 2) for 24 h. Cells were then dissociated with Accutase (ThermoFisher, A1110501), counted, and re-plated in the triple coated dish containing EM grids described below (Day 3-seeding day), and maintained in Neurobasal medium (ThermoFisher, 21103049) containing B-27 w/o Vitamin A (Gibco, 12587010), GlutaMAX (ThermoFisher 35050061), 200 µM of L-Ascorbic Acid (Sigma, A5960), 1 µM of DAPT (Tocris, 2634), 1 µg/ml puromycin, and 1µg/ml doxycycline. The triple coating is composed of 0.1 mg/mL of Poly-D-Lysine (Sigma, P0899), 10 µL/mL of Laminin (Sigma, 11243217001), and 10 µL/mL of Fibronectin (Sigma, F0895). Cells were cultured for two more days with 1 µg/µL puromycin and 1 µg/ml doxycycline (Day 5). Half of the medium was changed every two days without puromycin and doxycycline until the induced neurons were vitrified (Day 9).

Lentivirus generation

Two lentivirus plasmids from a published study (Ho et al., 2016), each containing hNGN2-P2A-eGFP-T2A-PuroR under the control of TetO promoter (Addgene 79823) and reverse tetracycline activator (rtTA) (Addgene 19780), were used to produce transgenes. Lentivirus was generated by co-transfecting transgene plasmid with two helper plasmids, pMD2 (Addgene 12259) and psPAX2 (Addgene 12260), by calcium phosphate transfection kit (Takara, 631312) following the manufacturer's protocol into HEK293 cells. After 48-72 h of incubation, media containing lentiviruses were harvested and concentrated at 112,000 g for 3 h, aliquoted, and stored at -80°C.

EM Grid micro-patterning

Gold (Au) 200-mesh grids with a holey 12 nm thick film made of SiO2 (R1/4, hole size/spacing in µm, Quantifoil Micro Tools), were micro-patterned (Toro-Nahuelpan et al., 2020). Briefly, grids were plasma cleaned on both sides at 100 W power with a 10 cm^3 per min flow rate of oxygen gas for 30–40 s (Diener Femto Plasma, DienerElectronic). Next, grids were incubated on droplets of poly-l-lysine grafted with polyethylene glycol (PLL(20)- g[3.5]-PEG(5), SuSoS AG) at a concentration of 0.5 mg/mL in 10 mM HEPES pH 7.4, for 1h at room temperature on parafilm in a humid chamber. Following passivation, the grids were blotted with filter paper from the back,

allowed to dry for few seconds and immediately placed on a drop of PLPP (4-benzoylbenzyl-trimethylammonium chloride, 14.5 mg/mL) in a sealed glass bottom ibidi µ-Dish 35mm low (ibidi). Grids were immediately micro-patterned using a DMD-based illumination (Primo, Alvéole Lab), applying a dose of 1,500 mJ/mm^2. Grids were promptly retrieved from the PLPP solution, washed in a 1,000 µL drop of water and two consecutive washes in 300 µL drops of PBS supplemented with Ca and Mg. Patterned grids were stored wet in PBS supplemented with Ca and Mg at 4 °C in a humid chamber. For functionalization of the micropatterns, grids were incubated at room temperature for 30 min in a 20 µL drop of 50 µg/mL laminin (Sigma, 11243217001) and 50 µg/mL fibronectin (ThermoFischer Scientific) in PBS supplemented with Ca and Mg. Grids were then washed three times in 300 µL drops of the corresponding buffer and stored at 4 °C in a humid chamber until use. hiPSC cells were seeded on laminin/fibronectin micro-patterned grids at a density of 2×10^4 cells per cm^2 in a glass bottom ibidi µ-Dish 35mm high (ibidi), and incubated for 48 h in this dish. In parallel, another glass bottom ibidi µ-Dish 35mm high (ibidi) was seeded with 2×10^5 cells per cm^2 (without grids). After 48 h, the grids were transferred (from the 2×10^4 cells per cm^2 seeded dish) to the 2×10^5 cells per cm^2 seeded dish. Neurons were grown for 6 days post-seeding with half-media change every 2 days. Grids were plunged on day 6 post-seeding using a Leica GP plunger at a 70% humidity and blotted for 1.5 sec, no nanogold fiducials were added.

Micropattern design

Micropatterns were designed in Inkscape (http://www.inkscape.org/) as 8-bit binary files and exported as .png files, which can be loaded into the Leonardo software v.4.12 (Alvéole Lab). Neuronal circuits micropatterns used for hiPSCs were designed such that 10 µm circles were patterned at the center of the grid square to direct cell body attachment. Circles were connected alternatingly with straight or curly lines (10 µm wide) to facilitate extension of neuronal process. Micro-patterned circuit covered an area of 10 x 8 grid squares (in a 200-mesh grid).

Cryo-TEM and tomography

Tilt series were collected on a Titan Krios (ThermoFisher Scientific) microscope operated at 300 kV equipped with a field-emission gun, a Quantum post-column energy filter (Gatan) operated in the zero-loss mode, a K2 Summit direct detector camera (Gatan) operated in counting mode and a Volta phase plate (VPP) (Thermo Fisher). The slit width of the energy filter was set to 20 eV. All the data were recorded with SerialEM software between -60º to 60º with a 2º increment.

Tilt series of primary neurons were acquired either with dose-symmetric (Hagen et al., 2017) or asymmetric bi-directional tilt scheme and a nominal defocus ranging from -2 to -6 µm at an EFTEM

magnification of ×64,000 resulting in pixel size of 2.24 Å. 60 tomograms were processed for subsequent structural analysis.

Tilt series of hiPSC-derived neurons were collected with dose symmetric scheme (Hagen et al., 2017) an EFTEM magnification of ×64,000 corresponding to pixel size at the specimen level of 2.129 Å, 2.5–4µm defocus, with constant dose for all tilts, total dose under 150 e/Å^2. Tilt-series were acquired with the VPP. 8 tomograms were processed for subsequent structural analysis.

A total 46 of bi-directional tilt-series corresponding to pluripotent control, Taxol-treated and nocodazole-treated P19 cells was collected at ×42,000 resulting in pixel size of 3.42 Å using VPP with a target defocus of 0-200 nm. A total of 35 dose-symmetric tilt series corresponding to pluripotent and differentiated P19 cells was also collected with an EFTEM magnification of ×64,000 corresponding to pixel size 2.24 Å and 2-5 µm defocus. In all cases, cumulative dose ranges between 90-120 e/Å^2. Mitotic HeLa cell tomograms were collected at ×33,000 resulting in pixel size of 4.21 Å using VPP with a target defocus of 0 nm.

Alignment and operation of the Volta phase plate were essentially carried out as described by Fukuda *et al.* (Fukuda et al., 2015), applying a beam tilt of 10mrad for autofocusing. Gain references were collected prior to data acquisition.

Processing of tilt-series

For preprocessing of tilt series, a MATLAB based custom tomoman package was used. Frames were first sorted followed by motion correction using MontionCor2 (Zheng et al., 2017) with 3 × 3 patches. Bad frames were then omitted from the motion corrected stacks. Frames were exposure filtered according to their cumulative electron dose. Defocus parameters were determined using GCTF 1.06 (Zhang, 2016) or CTFFIND 4.1.14 (Rohou and Grigorieff, 2015) on unfiltered stacks. For high resolution data processing, 3D defocus gradients in primary neuron and P19 tomograms were corrected in NovaCTF (Turoňová et al., 2017). CTF correction via phase-flipping used a Z-slab thickness of 15 nm. The resulting tomograms were consecutively binned via Fourier cropping. Preprocessing of hiPSC data were performed using Warp 1.7.b (Tegunov and Cramer, 2019) including frame alignment, gain correction, dose filtering, tilt sorting, and CTF fitting. In-focus tomograms collected with VPP were not CTF corrected. In all cases, the dose-filtered stacks were aligned with patch tracking in the IMOD software package (Kremer et al., 1996). Final alignment of the tilt-series images was performed using the linear interpolation option in IMOD without CTF correction. For tomographic reconstruction by back-projection, the radial filter options were left at their default values (cut off, 0.35; fall off, 0.05). Missing wedge compensated and

denoised cross-section of the tomogram represented in Figure S1A was prepared for visualization purpose using IsoNet (Liu et al., 2021).

MT tracing and curvature measurement

MT segmentations were performed with the automated module in Amira software v.6.2.0 (FEI Visualization Sciences Group) as described before (Chakraborty et al., 2020b) in the IMOD reconstructed tomograms using a generic missing wedge-modulated hollow cylinder with outer and inner radii of 14 and 7 nm, respectively and 120 nm length as a template. The coordinates of the traced filaments were resampled in MATLAB (MathWorks) to obtain equidistant points. MT curvature was determined by measuring the tangent-correlation length as described in our previous work (Chakraborty et al., 2020b). Data analysis was done by fitting a linear regression line in Origin 9.2 (OriginLab, Northampton, MA) on the data points obtained from each tomogram. $^{a}L_p$ values were calculated from the inverse slopes of the linear regression lines. Goodness of fits were determined from the Adjusted-R^2 values.

Density tracing and particle picking

For density tracing and particle picking, tomograms were smoothed by Gaussian low-pass filtering at σ_v=0.5 pixels and MT lumen is segmented based on the MT centerline tracing. Densities within the lumen were traced in 3D using a discrete Morse theory based software package PySeg (Martinez-Sanchez et al., 2020). Briefly, grayscale minima positions were identified and the most relevant ones were preserved by topological persistence simplification, while discarding those generated from noise or spurious densities. Next, mean shift clustering method (Comaniciu and Meer, 2002) with 6 nm bandwidth was applied that allowed detection of particles and particle picking within MT lumen in an unbiased template-free way. The persistence threshold was set for picking all lumenal particles independent of the type of density. Therefore, this threshold was adjusted for having the same density of minima at the shell for every MT, specifically 0.004 vertices/nm^3 for phase plate tomograms and 0.006 vertices/nm^3 for the defocus tomograms.

Particle concentration measurements

Lumenal particle concentrations present in different neuronal samples were measured by counting traced particles obtained by PySeg within each MT of the corresponding samples. Prior to counting all particle, coordinates were refined in RELION. Similarly, concentrations of the individual class averages were determined by counting their occurrences in each MT across

tomograms. In all cases, lumen radius was set to 6 nm and MT length was obtained from the segmentations. MTs with length less than 100 nm was excluded from the analysis.

Subtomogram averaging

All analysis steps were performed using REgularised LIkelihood OptimisatioN (RELION) (version 3.0.5) following published protocols (Zivanov et al., 2018). During the refinement, particle half-datasets were processed independently according to the “gold standard” procedure, as implemented in RELION. Unless stated explicitly, all refinements were performed *de novo*, that is, without the use of external references. Datasets corresponding to different cells were processed separately.

Lumenal particle sub-tomograms from the coordinates determined by the automated particle picking algorithm were extracted at 1x binning (2.24 Å/pix for all data, except 2.129 Å/pix in case of hiPSC data) within a box size of 128 pixels^3. For VPP data, no CTF correction was performed and lumenal particle sub-tomograms were reconstructed using IMOD (3.42 Å/pix and 4.21 Å/pix) within a box size of 128 pixels^3. For P19 cell data, we have mixed only VPP datasets from different conditions to increase the particle number as well as to get better angular sampling. All the subtomograms correspond to side views only and lacked views from cross-sections. Individual particles have different orientation within MT lumen helped mitigate this problem. For primary neuronal and hiPSC-derived neuronal data sets, we extracted about 50k and 8k particles respectively. They were first 3D auto-refined in RELION followed by sorting into different classes using 3D classification. For the 3D classification, particle alignment was skipped and large number of classes (>10) were used to pick up small differences. Individual classes were then 3D auto-refined using global search parameters and further classified. We followed this procedure iteratively until homogeneous classes were obtained. Finally, the class averages were locally refined using a soft particle mask and post processed to determine gold standard FSC curve. Reproducibility of the class averages validated using a simple sphere or cylinder as initial references. In all cases, data converged to a single solution indicating these class averages are indeed the global minima. In order to substantiate, we calculated cross-correlations between the solutions obtained from the different initial models in Chimera (v1.15) (Pettersen et al., 2004) and represented in **Fig S6**. Cross-correlations between the maps were obtained using ‘fit’ command in the command line and further refined using ‘fit in map’ from the menu.

Polarity determination of MTs

Resampled coordinates of the primary neuronal MTs extracted from Amira were used to make a tubular grid in MATLAB by placing points on each tubulin subunits having inter-subunit distance of 40 Å along the filament z-axis and 60 Å around the helix. These positions were oversampled 2x-times and subtomograms were extracted from these grid points. Subtomograms extracted from the same filament were assigned a class number which helped in determination MT polarity. Subtomogram averaging was performed in STOPGAP (Wan et al., 2020). An initial reference was generated *de novo* from a single MT filament. 20,259 subtomograms were extracted from the resampled positions using a binning factor of 2 (8.96 Å/pixel) and a box size of 64 pixels^3 and a starting reference was generated by averaging all sub-tomograms. Due to in-plane randomization, the initial structure resembles a featureless cylinder. Several rounds of global alignment of the in-plane angle followed by local refinement of all Euler angles were conducted. Shift refinements were limited to 4 and 6 nm in x- and y- direction along the filament centerline. This averaging approach resulted in the emergence of the helical pattern of the MT (**Fig. S1B,E**). We used this optimized starting model for refining the whole data set for 5-10 iterations. In order to determine the polarity of the MTs, each MT in the dataset was averaged separately using multiclass averaging and subtomogram orientations were visualized in Chimera as lattice maps using 'place object' plugin (Qu et al., 2018). Polarities were sorted out using visual inspection and in-plane angles in the motive list were changed by 180°. Unbinned subtomogram were extracted using a box size of 96^3 pixels^3 and aligned iteratively, resulting in a refined structure of MT at a resolution of 8.2 Å. For fitting tubulin dimer (PDB**: 1tub)** into the obtained structure, we used Chimera for rigid body fitting however, fitting was not optimal. Therefore, we used qwikMD (Ribeiro et al., 2016) with default parameters for flexible fitting of tubulin dimer and represented in **Fig.1C**.

Mass measurement of lumenal particles

The luminal particles with a voxel size of 3.42 Å were filtered using a circular kernel (TomToolbox, tom_filter kernel=6). The threshold for binarization was determined by measuring the mass of the ribosome particles from the same tomogram. The threshold was decreased until the mean mass of all ribosome particles was ~3.6 MDa, and then applied to the luminal particles for binarization. To correct for the different contrast regimes a fudge factor of 0.5 applied to the threshold. Binarized luminal particles were segmented using Matlab's regionprops3, yielding the number of voxels for the biggest object inside one subvolume. The corresponding mass of each particle was calculated based on voxel size and the protein density (1.3 g cm^{-3}).

Template matching

To generate a subtomogram average of the ribosomes present in the neurons and P19 cells, ribosomes were localized by template matching in PyTom (Hrabe et al., 2012). As a template, we used the 4 nm down filtered structures of 80S ribosome (EMD: 1480) rescaled to the tomogram pixel size. False positives were identified by constrained cross-correlation (CCC) histogram which showed well separated peaks for the true and false positives (**Fig. S5C**). However, picked positions were manually verified again. In case of P19 ribosomes, 5553 unbinned subtomograms were extracted at the detected coordinates and refined in RELION which converged into a ribosome density (**Fig. S5D**). Particles were next sorted in 3D classification steps in RELION to remove remaining false positives and junks. After final refinement and post processing we obtained a density map at 18 Å resolution (**Fig. S5E**) from 4723 particles. In case of neuronal ribosomes, 975 4x-binned subtomograms centered on the identified coordinates were extracted and refined in RELION using a data driven template. The refinement converged into a ribosome density. The data was further classified to remove junk. All the good classes were combined and un-binned sequentially to 2x and 1x and final refinement gave 28 Å resolution ribosome average.

Polyribosome detection

Polyribosome detection was essentially based on hierarchical transformation clustering as described recently in Jiang et al. (Jiang et al., 2022). The algorithm considered the directions of the transformations (rotations and translations). The method consists of 3 major steps: (i) transformations (rotations, translations) between ribosome pairs were calculated; (ii) distance matrices for rotations and translations were computed and combined; (iii) transformations were clustered based on the combined distance matrix (**Fig. S5G-I**).

Heat Map

Heat Maps were calculated by generating a volume of zeros with the size of the analyzed tomograms (928x928x500 voxels). For each particle position, the voxel value in the empty volume was set to 1. The 3D heat map was calculated by moving a spherical kernel with 2x radius of the particle over the volume. The mean for each kernel position was determined. Finally the 3D heat map was projected in z.

Spatial statistics

We computed 1st order univariate (NN-distance) and 2nd order bivariate (Ripley's L) functions for spatial statistical analysis of 3D lumenal particles in a cellular compartment (MT lumen) as

proposed in (Martinez-Sanchez et al., 2020). The detailed description of the numerical corrections needed for successfully computation of these functions from cryo-ET data is described in Martinez-Sanchez et al (Martinez-Sanchez et al., 2022). Protein localizations, angular orientations and 3D shapes were taken from STA, MTs lumen were segmented from the traced MT centerlines and a assuming a radius section of 6 nm. Completely Spatial Randomness with Volume exclusion synthetic patterns (CSRV) were used as null-models in all cases, we simulated 20 instances for each MT to construct the interval of confidences for null-models. One sided Welch tests are used to discard the next null-hypothesis: experimental particle density has the same mean than the CSRV case at a specific distance to a reference point (MT plus end or breakpoint).

Statistical analysis

Statistical analyses were performed with Origin 9.2. All boxes in the box-plot representations are bound by the 25th–75th percentile, whiskers span 5th to 95th percentile. Mean values were marked by a black box. Box plots are embedded inside a violin which indicate distribution of the data. For statistical significance, nonparametric Mann-Whitney tests were performed unless stated otherwise. Significances were indicated by stars where ** indicated $P<0.01$.

Visualization and analysis of sub-tomogram analysis results

RELION and STOPGAP post-processing were used to calculate FSC and perform B factor sharpening as stated in the Methods. UCSF Chimera (Pettersen et al., 2004) was used for visualization and figure generation. Numerical data and statistics were analyzed in Origin software. Quantification and plots were done in MATLAB (R2015b, The Mathworks, Inc. Massachusetts, USA). Particle picking and density tracing were visualized using Paraview. Molecular model fitting was performed in Chimera (Pettersen et al., 2004). Models were fit into non-segmented density maps using fit command from the command line in an unbiased manner. Since TBCD model is the largest and has distinct shape, it was always fitted first. The 30 most probable fits were obtained. Highest cross-correlation hits were selected and refined using ‘fit in map’ command from the menu.

Affinity purification and Mass spectrometry based proteomics

HeLa Kyoto cells expressing GFP-tagged β-tubulin proteins from BAC transgenes (Poser et al., 2008) were grown to near-confluency on two 15-cm cell culture dishes per interaction experiment. DSS (Thermo Fisher Scientific, 21555) solution was prepared fresh in dry DMSO at a concentration of 20 mM concentration. Before crosslinking, cells were washed with ice-cold PBS (pH 8.0) to remove amine-containing culture media and extracellular proteins. DSS solution was

added at a final concentration of 5 mM for 30 mins. The reaction was quenched by 10 mM Tris-Cl for 15 mins at room temperature. Cells were collected by scraping and snap frozen in liquid N_2. Three replicates were harvested. Cell pellets were lysed with a buffer containing 0.1% NP-40 (Sigma) and subjected to affinity purification using anti-GFP antibodies immobilized on a magnetic beads (Miltenyi Biotec, 130-091-125). Purified proteins were digested sequentially with LysC and trypsin, desalted and subjected to mass spectrometric analysis on an Orbitrap instrument (Q Exactive HF) at mass spectrometry facility of Max-Planck institute of biochemistry. Raw files were processed with MaxQuant (Cox and Mann, 2008). MaxQuant output data was processed in Perseus (v.1.6.14.0) program with standard procedure (Tyanova et al., 2016). Protein identifications were filtered, removing hits to the reverse decoy database as well as proteins only identified by modified peptides. Protein LFQ intensities were logarithmized and missing values imputed by values simulating noise around the detection limit.

References

Afzelius, B.A. (1988). Microtubules in the spermatids of stick insects. J. Ultrastruct. Res. Mol. Struct. Res. *98*, 94–102.

Aher, A., Rai, D., Schaedel, L., Gaillard, J., John, K., Liu, Q., Altelaar, M., Blanchoin, L., Thery, M., and Akhmanova, A. (2020). CLASP Mediates Microtubule Repair by Restricting Lattice Damage and Regulating Tubulin Incorporation. Curr. Biol. *30*, 2175–2183.e6.

Akella, J.S., Wloga, D., Kim, J., Starostina, N.G., Lyons-Abbott, S., Morrissette, N.S., Dougan, S.T., Kipreos, E.T., and Gaertig, J. (2010). MEC-17 is an α-tubulin acetyltransferase. Nature *467*, 218–222.

Akhmanova, A., and Steinmetz, M.O. (2008). Tracking the ends: A dynamic protein network controls the fate of microtubule tips. Nat. Rev. Mol. Cell Biol. *9*, 309–322.

Al-Bassam, J., Ozer, R.S., Safer, D., Halpain, S., and Milligan, R.A. (2002). MAP2 and tau bind longitudinally along the outer ridges of microtubule protofilaments. J. Cell Biol. *157*, 1187–1196.

Amos, L.A., and Schlieper, D. (2005). Microtubules and maps. Adv. Protein Chem. *71*, 257–298.

Atherton, J., Stouffer, M., Francis, F., and Moores, C.A. (2018). Microtubule architecture in vitro and in cells revealed by cryo-electron tomography. Acta Crystallogr. Sect. D Struct. Biol. *74*, 572–584.

Bassot, J.M., and Martoja, R. (1966). Données histologiques et ultrastructurales sur les microtubules cytoplasmiques du canal éjaculateur des insectes orthoptères. Zeitschrift Für Zellforsch. Und Mikroskopische Anat. *74*, 145–181.

Behnke, O. (1967). Incomplete microtubules observed in mammalian blood platelets during microtubule polymerization. J. Cell Biol. *34*, 697–701.

Bentley, M., and Banker, G. (2016). The cellular mechanisms that maintain neuronal polarity. Nat. Rev. Neurosci. *17*, 611–622.

Bhamidipati, A., Lewis, S. a., and Cowan, N.J. (2000). ADP ribosylation factor-like protein 2 (Arl2) regulates the interaction of tubulin-folding cofactor D with native tubulin. J. Cell Biol. *149*, 1087–1096.

Bodakuntla, S., Jijumon, A.S., Villablanca, C., Gonzalez-Billault, C., and Janke, C. (2019). Microtubule-Associated Proteins: Structuring the Cytoskeleton. Trends Cell Biol. *29*, 804–819.

Bouchet-Marquis, C., Zuber, B., Glynn, A.-M., Eltsov, M., Grabenbauer, M., Goldie, K.N., Thomas, D., Frangakis, A.S., Dubochet, J., and Chrétien, D. (2007). Visualization of cell microtubules in their native state. Biol. Cell *99*, 45–53.

Bulinski, J.C. (2019). Microtubules and Neurodegeneration: The Tubulin Code Sets the Rules of the Road. Curr. Biol. *29*, R28–R30.

Burton, P.R. (1984). Luminal material in microtubules of frog olfactory axons: structure and distribution. J. Cell Biol. *99*, 520–528.

Campenot, R.B., Lund, K., and Senger, D.L. (1996). Delivery of newly synthesized tubulin to rapidly growing distal axons of rat sympathetic neurons in compartmented cultures. J. Cell Biol. *135*, 701–709.

Chakraborty, S., Jasnin, M., and Baumeister, W. (2020a). Three-dimensional organization of the cytoskeleton: A cryo-electron tomography perspective. Protein Sci. *29*, 1302–1320.

Chakraborty, S., Mahamid, J., and Baumeister, W. (2020b). Cryoelectron Tomography Reveals Nanoscale Organization of the Cytoskeleton and Its Relation to Microtubule Curvature Inside Cells. Structure *28*, 991–1003.e4.

Comaniciu, D., and Meer, P. (2002). Mean shift: A robust approach toward feature space analysis. IEEE Trans. Pattern Anal. Mach. Intell. *24*, 603–619.

Coombes, C., Yamamoto, A., McClellan, M., Reid, T.A., Plooster, M., Luxton, G.W.G., Alper, J., Howard, J., and Gardner, M.K. (2016). Mechanism of microtubule lumen entry for the α-tubulin acetyltransferase enzyme αTAT1. Proc. Natl. Acad. Sci. U. S. A. *113*, E7176–E7184.

Cooper, J.A. (2013). Cell biology in neuroscience: mechanisms of cell migration in the nervous system. J. Cell Biol. *202*, 725–734.

Cox, J., and Mann, M. (2008). MaxQuant enables high peptide identification rates, individualized p.p.b.-range mass accuracies and proteome-wide protein quantification. Nat. Biotechnol. *26*, 1367–1372.

Cuveillier, C., Delaroche, J., Seggio, M., Gory-Fauré, S., Bosc, C., Denarier, E., Bacia, M., Schoehn, G., Mohrbach, H., Kulić, I., et al. (2020). MAP6 is an intraluminal protein that induces neuronal microtubules to coil. Sci. Adv. *6*, eaaz4344.

Cyrklaff, M., Kudryashev, M., Leis, A., Leonard, K., Baumeister, W., Menard, R., Meissner, M., and Frischknecht, F. (2007). Cryoelectron tomography reveals periodic material at the inner side of subpellicular microtubules in apicomplexan parasites. J. Exp. Med. *204*, 1281–1287.

Davis, L.J., Odde, D.J., Block, S.M., and Gross, S.P. (2002). The importance of lattice defects in katanin-mediated microtubule severing in vitro. Biophys. J. *82*, 2916–2927.

Dent, E.W., Gupton, S.L., and Gertler, F.B. (2011). The growth cone cytoskeleton in Axon outgrowth and guidance. Cold Spring Harb. Perspect. Biol. *3*, 1–39.

Drewes, G., Ebneth, A., and Mandelkow, E.M. (1998). MAPs, MARKs and microtubule dynamics. Trends Biochem. Sci. *23*, 307–311.

Echandía, E.L.R., Piezzi, R.S., and Rodríguez, E.M. (1968). Dense-core microtubules in neurons and gliocytes of the toad Bufo arenarum Hensel. Am. J. Anat. *122*, 157–167.

Falconer, M.M., Vielkind, U., and Brown, D.L. (1989a). Establishment of a stable, acetylated microtubule bundle during neuronal commitment. Cell Motil. Cytoskeleton *12*, 169–180.

Falconer, M.M., Vielkind, U., and Brown, D.L. (1989b). Association of acetylated microtubules, vimentin intermediate filaments, and MAP 2 during early neural differentiation in EC cell culture. Biochem. Cell Biol. *67*, 537–544.

Ferro, L.S., Eshun-Wilson, L., Gölcük, M., Fernandes, J., Huijben, T., Gerber, E., Jack, A., Costa, K., Gür, M., Fang, Q., et al. (2020). The mechanism of motor inhibition by microtubule-associated proteins. bioRxiv 2020.10.22.351346.

Foster, H.E., Ventura Santos, C., and Carter, A.P. (2022). A cryo-ET survey of microtubules and intracellular compartments in mammalian axons. J. Cell Biol. *221*, e202103154.

Francis, J.W., Newman, L.E., Cunningham, L.A., and Kahn, R.A. (2017). A trimer consisting of the Tubulin-specific Chaperone D (TBCD), regulatory GTPase ARL2, and β-tubulin is required for maintaining the microtubule network. J. Biol. Chem. *292*, 4336–4349.

Fukuda, Y., Laugks, U., Lučić, V., Baumeister, W., and Danev, R. (2015). Electron cryotomography of vitrified cells with a Volta phase plate. J. Struct. Biol. *190*, 143–154.

Gaertig, J., and Wloga, D. (2012). Microtubules: MEC-17 Moonlights in the Lumen. Curr. Biol. *22*, R483–R485.

Garvalov, B.K., Zuber, B., Bouchet-Marquis, C., Kudryashev, M., Gruska, M., Beck, M., Leis, A., Frischknecht, F., Bradke, F., Baumeister, W., et al. (2006). Luminal particles within cellular microtubules. J. Cell Biol. *174*, 759–765.

Grünewald, K., Desai, P., Winkler, D.C., Heymann, J.B., Belnap, D.M., Baumeister, W., and Steven, A.C. (2003). Three-Dimensional Structure of Herpes Simplex Virus from Cryo-Electron Tomography. Science *302*, 1396–1398.

Hagen, W.J.H., Wan, W., and Briggs, J.A.G. (2017). Implementation of a cryo-electron tomography tilt-scheme optimized for high resolution subtomogram averaging. J. Struct. Biol. *197*, 191–198.

Hirokawa, N., Niwa, S., and Tanaka, Y. (2010). Molecular Motors in Neurons: Transport Mechanisms and Roles in Brain Function, Development, and Disease. Neuron *68*, 610–638.

Ho, S.-M., Hartley, B.J., TCW, J., Beaumont, M., Stafford, K., Slesinger, P.A., and Brennand, K.J. (2016). Rapid Ngn2-induction of excitatory neurons from hiPSC-derived neural progenitor cells. Methods *101*, 113–124.

Hoffmann, P.C., Giandomenico, S.L., Ganeva, I., Wozny, M.R., Sutcliffe, M., Lancaster, M.A., and Kukulski, W. (2021). Electron cryo-tomography reveals the subcellular architecture of growing axons in human brain organoids. Elife *10:e70269*.

Hrabe, T., Chen, Y., Pfeffer, S., Kuhn Cuellar, L., Mangold, A.V., and Förster, F. (2012). PyTom: A python-based toolbox for localization of macromolecules in cryo-electron tomograms and subtomogram analysis. J. Struct. Biol. *178*, 177–188.

Ichikawa, M., and Bui, K.H. (2018). Microtubule Inner Proteins: A Meshwork of Luminal Proteins Stabilizing the Doublet Microtubule. BioEssays *40*, 1700209.

Ichikawa, M., Khalifa, A.A.Z., Kubo, S., Dai, D., Basu, K., Maghrebi, M.A.F., Vargas, J., and Bui, K.H. (2019). Tubulin lattice in cilia is in a stressed form regulated by microtubule inner proteins. Proc. Natl. Acad. Sci. U. S. A. *116*, 19930–19938.

Javier-Torrent, M., Zimmer-Bensch, G., and Nguyen, L. (2021). Mechanical Forces Orchestrate Brain Development. Trends Neurosci. *44*, 110–121.

Jaworski, J., Kapitein, L.C., Gouveia, S.M., Dortland, B.R., Wulf, P.S., Grigoriev, I., Camera, P., Spangler, S. a., Di Stefano, P., Demmers, J., et al. (2009). Dynamic Microtubules Regulate Dendritic Spine Morphology and Synaptic Plasticity. Neuron *61*, 85–100.

Jiang, W., Wagner, J., Du, W., Plitzko, J., Baumeister, W., Beck, F., and Guo, Q. (2022). A transformation clustering algorithm and its application in polyribosomes structural profiling. Nucleic Acids Res. *gkac547*, https://doi.org/10.1093/nar/gkac547.

Jumper, J., Evans, R., Pritzel, A., Green, T., Figurnov, M., Ronneberger, O., Tunyasuvunakool, K., Bates, R., Žídek, A., Potapenko, A., et al. (2021). Highly accurate protein structure prediction with AlphaFold. Nature *596*, 583–589.

Katrukha, E.A., Jurriens, D., Salas Pastene, D.M., and Kapitein, L.C. (2021). Quantitative mapping of dense microtubule arrays in mammalian neurons. Elife *10:e67925*.

Kellogg, E.H., Hejab, N.M.A., Poepsel, S., Downing, K.H., DiMaio, F., and Nogales, E. (2018). Near-atomic model of microtubule-tau interactions. Science *360*, 1242–1246.

Kremer, J.R., Mastronarde, D.N., and McIntosh, J.R. (1996). Computer visualization of three-dimensional image data using IMOD. J. Struct. Biol. *116*, 71–76.

Larti, F., Kahrizi, K., Musante, L., Hu, H., Papari, E., Fattahi, Z., Bazazzadegan, N., Liu, Z., Banan, M., Garshasbi, M., et al. (2015). A defect in the CLIP1 gene (CLIP-170) can cause autosomal recessive intellectual disability. Eur. J. Hum. Genet. *23*, 331–336.

Lasek, R.J., Dabrowski, C., and Nordlander, R. (1973). Analysis of axoplasmic RNA from invertebrate giant axons. Nat. New Biol. *244*, 162–165.

LeDizet, M., and Piperno, G. (1987). Identification of an acetylation site of Chlamydomonas alpha-tubulin. Proc. Natl. Acad. Sci. U. S. A. *84*, 5720–5724.

Lewis, S.A., Tian, G., and Cowan, N.J. (1997). The [alpha]- and [beta]-tubulin folding pathways. Trends Cell Biol. *7*, 479–484.

Li, Z., Jaroszewski, L., Iyer, M., Sedova, M., and Godzik, A. (2020). FATCAT 2.0: Towards a better understanding of the structural diversity of proteins. Nucleic Acids Res. *48*, W60–W64.

Liu, Y.-T., Zhang, H., Wang, H., Tao, C.-L., Bi, G.-Q., and Zhou, Z.H. (2021). Isotropic Reconstruction of Electron Tomograms with Deep Learning. bioRxiv doi:10.1101/2021.07.17.452128.

Lučić, V., Kossel, A.H., Yang, T., Bonhoeffer, T., Baumeister, W., and Sartori, A. (2007). Multiscale imaging of neurons grown in culture: From light microscopy to cryo-electron tomography. J. Struct. Biol. *160*, 146–156.

Lučić, V., Rigort, A., and Baumeister, W. (2013). Cryo-electron tomography: The challenge of doing structural biology in situ. J. Cell Biol. *202*, 407–419.

Lundin, V.F., Leroux, M.R., and Stirling, P.C. (2010). Quality control of cytoskeletal proteins and human disease. Trends Biochem. Sci. *35*, 288–297.

Mahamid, J., Pfeffer, S., Schaffer, M., Villa, E., Danev, R., Kuhn Cuellar, L., Forster, F., Hyman, A.A., Plitzko, J.M., and Baumeister, W. (2016). Visualizing the molecular sociology at the HeLa cell nuclear periphery. Science *351*, 969–972.

Manka, S.W., and Moores, C.A. (2018). Microtubule structure by cryo-EM: Snapshots of dynamic instability. Essays Biochem. *62*, 737–751.

Martinez-Sanchez, A., Kochovski, Z., Laugks, U., Meyer zum Alten Borgloh, J., Chakraborty, S., Pfeffer, S., Baumeister, W., and Lučić, V. (2020). Template-free detection and classification of membrane-bound complexes in cryo-electron tomograms. Nat. Methods *17*, 209–216.

Martinez-Sanchez, A., Baumeister, W., and Lučić, V. (2022). Statistical spatial analysis for cryo-electron tomography. Comput. Methods Programs Biomed. *218*, 106693.

Matsuyama, A., Shimazu, T., Sumida, Y., Saito, A., Yoshimatsu, Y., Seigneurin-Berny, D., Osada, H., Komatsu, Y., Nishino, N., Khochbin, S., et al. (2002). In vivo destabilization of dynamic microtubules by HDAC6-mediated deacetylation. EMBO J. *21*, 6820–6831.

Nithianantham, S., Le, S., Seto, E., Jia, W., Leary, J., Corbett, K.D., Moore, J.K., and Al-Bassam, J. (2015). Tubulin cofactors and Arl2 are cage-like chaperones that regulate the soluble αβ-tubulin pool for microtubule dynamics. Elife *4:e08811*.

Nogales, E., Whittaker, M., Milligan, R.A., and Downing, K.H. (1999). High-resolution model of the microtubule. Cell *96*, 79–88.

Nomura, M., Atsuji, K., Hirose, K., Shiba, K., Yanase, R., Nakayama, T., Ishida, K., and Inaba, K. (2019). Microtubule stabilizer reveals requirement of Ca2+-dependent conformational changes of microtubules for rapid coiling of haptonema in haptophyte algae. Biol. Open *8*, bio036590.

Odde, D. (1998). Diffusion inside microtubules. Eur. Biophys. J. *27*, 514–520.

Owa, M., Uchihashi, T., Yanagisawa, H., Yamano, T., Iguchi, H., Fukuzawa, H., Wakabayashi, K., Ando, T., and Kikkawa, M. (2019). Inner lumen proteins stabilize doublet microtubules in cilia and flagella. Nat. Commun. *10*, 1143.

Pettersen, E.F., Goddard, T.D., Huang, C.C., Couch, G.S., Greenblatt, D.M., Meng, E.C., and Ferrin, T.E. (2004). UCSF Chimera?A visualization system for exploratory research and analysis. J. Comput. Chem. *25*, 1605–1612.

Portran, D., Schaedel, L., Xu, Z., Théry, M., and Nachury, M.V. (2017). Tubulin acetylation protects long-lived microtubules against mechanical ageing. Nat. Cell Biol. *19*, 391–398.

Poser, I., Sarov, M., Hutchins, J.R.A., Hériché, J.K., Toyoda, Y., Pozniakovsky, A., Weigl, D., Nitzsche, A., Hegemann, B., Bird, A.W., et al. (2008). BAC TransgeneOmics: A high-throughput method for exploration of protein function in mammals. Nat. Methods *5*, 409–415.

Qu, K., Glass, B., Dolezal, M., Schur, F.K.M., Murciano, B., Rein, A., Rumlová, M., Ruml, T., Kräusslich, H.G., and Briggs, J.A.G. (2018). Structure and architecture of immature and mature murine leukemia virus capsids. Proc. Natl. Acad. Sci. U. S. A. *115*, E11751–E11760.

Reber, S., and Hyman, A.A. (2015). Emergent Properties of the Metaphase Spindle. Cold Spring Harb. Perspect. Biol. *7*, a015784.

Ribeiro, J. V., Bernardi, R.C., Rudack, T., Stone, J.E., Phillips, J.C., Freddolino, P.L., and Schulten, K. (2016). QwikMD — Integrative Molecular Dynamics Toolkit for Novices and Experts. Sci. Rep. *6*, 26536.

Rigort, A., Günther, D., Hegerl, R., Baum, D., Weber, B., Prohaska, S., Medalia, O., Baumeister, W., and Hege, H.C. (2012). Automated segmentation of electron tomograms for a quantitative description of actin filament networks. J. Struct. Biol. *177*, 135–144.

Rohou, A., and Grigorieff, N. (2015). CTFFIND4: Fast and accurate defocus estimation from electron micrographs. J. Struct. Biol. *192*, 216–221.

Scheres, S.H.W. (2012). RELION: Implementation of a Bayesian approach to cryo-EM structure determination. J. Struct. Biol. *180*, 519–530.

Schrod, N., Vanhecke, D., Laugks, U., Stein, V., Fukuda, Y., Schaffer, M., Baumeister, W., and Lučić, V. (2018). Pleomorphic linkers as ubiquitous structural organizers of vesicles in axons. PLoS One *13*, e0197886.

Serna, M., Carranza, G., Martín-Benito, J., Janowski, R., Canals, A., Coll, M., Zabala, J.C., and Valpuesta, J.M. (2015). The structure of the complex between α-tubulin, TBCE and TBCB reveals a tubulin dimer dissociation mechanism. J. Cell Sci. *128*, 1824–1834.

Srayko, M., O'Toole, E.T., Hyman, A.A., and Müller-Reichert, T. (2006). Katanin Disrupts the Microtubule Lattice and Increases Polymer Number in C. elegans Meiosis. Curr. Biol. *16*, 1944–1949.

Srivastava, A.K., and Schwartz, C.E. (2014). Intellectual disability and autism spectrum disorders: Causal genes and molecular mechanisms. Neurosci. Biobehav. Rev. *46*, 161–174.

Subramanian, R., and Kapoor, T.M. (2012). Building Complexity: Insights into Self-Organized Assembly of Microtubule-Based Architectures. Dev. Cell *23*, 874–885.

Tegunov, D., and Cramer, P. (2019). Real-time cryo-electron microscopy data preprocessing with Warp. Nat. Methods *16*, 1146–1152.

Tian, G., and Cowan, N.J. (2013). Tubulin-specific chaperones: Components of a molecular machine that assembles the α/β heterodimer. Methods Cell Biol. *115*, 155–171.

Tian, G., Thomas, S., and Cowan, N.J. (2010). Effect of TBCD and its regulatory interactor Arl2 on tubulin and microtubule integrity. Cytoskeleton *67*, 706–714.

Topalidou, I., Keller, C., Kalebic, N., Nguyen, K.C.Q., Somhegyi, H., Politi, K.A., Heppenstall, P., Hall, D.H., and Chalfie, M. (2012). Genetically separable functions of the MEC-17 tubulin acetyltransferase affect microtubule organization. Curr. Biol. *22*, 1057–1065.

Toro-Nahuelpan, M., Zagoriy, I., Senger, F., Blanchoin, L., Théry, M., and Mahamid, J. (2020). Tailoring cryo-electron microscopy grids by photo-micropatterning for in-cell structural studies. Nat. Methods *17*, 50–54.

Turoňová, B., Schur, F.K.M., Wan, W., and Briggs, J.A.G. (2017). Efficient 3D-CTF correction for cryo-electron tomography using NovaCTF improves subtomogram averaging resolution to 3.4 Å. J. Struct. Biol. *199*, 187–195.

Tyanova, S., Temu, T., Sinitcyn, P., Carlson, A., Hein, M.Y., Geiger, T., Mann, M., and Cox, J. (2016). The Perseus computational platform for comprehensive analysis of (prote)omics data. Nat. Methods *13*, 731–740.

Vining, K.H., and Mooney, D.J. (2017). Mechanical forces direct stem cell behaviour in development and regeneration. Nat. Rev. Mol. Cell Biol. *18*, 728–742.

Wan, W., Khavnekar, S., Wagner, J., Erdmann, P., and Baumeister, W. (2020). STOPGAP: A Software Package for Subtomogram Averaging and Refinement. Microsc. Microanal. *26*, 2516–2516.

Xu, Z., Schaedel, L., Portran, D., Aguilar, A., Gaillard, J., Peter Marinkovich, M., Théry, M., and Nachury, M. V. (2017). Microtubules acquire resistance from mechanical breakage through intralumenal acetylation. Science *356*, 328–332.

Yau, K.W., Schätzle, P., Tortosa, E., Pagès, S., Holtmaat, A., Kapitein, L.C., and Hoogenraad, C.C. (2016). Dendrites In vitro and In vivo contain microtubules of opposite polarity and axon formation correlates with uniform plus-end-out microtubule orientation. J. Neurosci. *36*, 1071–1085.

Zhang, K. (2016). Gctf: Real-time CTF determination and correction. J. Struct. Biol. *193*, 1–12.

Zhang, Y., Pak, C.H., Han, Y., Ahlenius, H., Zhang, Z., Chanda, S., Marro, S., Patzke, C., Acuna, C., Covy, J., et al. (2013). Rapid single-step induction of functional neurons from human pluripotent stem cells. Neuron *78*, 785–798.

Zheng, S.Q., Palovcak, E., Armache, J.-P., Verba, K.A., Cheng, Y., and Agard, D.A. (2017). MotionCor2: anisotropic correction of beam-induced motion for improved cryo-electron microscopy. Nat. Methods *14*, 331–332.

Zilberman, Y., Ballestrem, C., Carramusa, L., Mazitschek, R., Khochbin, S., and Bershadsky, A. (2009). Regulation of microtubule dynamics by inhibition of the tubulin deacetylase HDAC6. J. Cell Sci. *122*, 3531–3541.

Zivanov, J., Nakane, T., Forsberg, B.O., Kimanius, D., Hagen, W.J.H., Lindahl, E., and Scheres, S.H.W. (2018). New tools for automated high-resolution cryo-EM structure determination in RELION-3. Elife *7:e42166*.